The Observed State of the Water Cycle in the Early 21st Century

By

M. Rodell[1]*, H.K. Beaudoing[1,2], T.S. L'Ecuyer[3], W.S. Olson[1,4], J.S. Famiglietti[5], P.R. Houser[6], R. Adler[2], M.G. Bosilovich[1], C.A. Clayson[7], D. Chambers[8], E. Clark[9], E.J. Fetzer[5], X. Gao[10], G. Gu[1,2], K. Hilburn[11], G.J. Huffman[1], D.P. Lettenmaier[9], W.T. Liu[5], F.R. Robertson[12], C.A. Schlosser[10], J. Sheffield[13], and E.F. Wood[13]

1. NASA Goddard Space Flight Center, Greenbelt, MD
2. Earth System Science Interdisciplinary Center, the University of Maryland, College Park
3. The University of Wisconsin, Madison
4. The University of Maryland, Baltimore County, MD
5. NASA Jet Propulsion Laboratory, Pasadena, CA
6. George Mason University, Fairfax, VA
7. Woods Hole Oceanographic Institute, Woods Hole, MA
8. The University of South Florida, St. Petersburg
9. The University of Washington, Seattle
10. Massachusetts Institute of Technology, Cambridge, MA
11. Remote Sensing Systems, Santa Rosa, CA
12. NASA Marshall Space Flight Center, Hunstville, AL
13. Princeton University, Princeton, NJ

*Corresponding Author address:
Hydrological Sciences Laboratory
Code 617, bldg 33, rm G227
NASA Goddard Space Flight Center
Greenbelt, MD 20771
Matthew.Rodell@nasa.gov

Submitted to Journal of Climate
7/16/14

Abstract

This study quantifies mean annual and monthly fluxes of Earth's water cycle over continents and ocean basins during the first decade of the millennium. To the extent possible, the flux estimates are based on satellite measurements first and data-integrating models second. A careful accounting of uncertainty in the estimates is included. It is applied within a routine that enforces multiple water and energy budget constraints simultaneously in a variational framework, in order to produce objectively-determined, optimized flux estimates. In the majority of cases, the observed annual, surface and atmospheric water budgets over the continents and oceans close with much less than 10% residual. Observed residuals and optimized uncertainty estimates are considerably larger for monthly surface and atmospheric water budget closure, often nearing or exceeding 20% in North America, Eurasia, Australia and neighboring islands, and the Arctic and South Atlantic Oceans. The residuals in South America and Africa tend to be smaller, possibly because cold land processes are a non-issue. Fluxes were poorly observed over the Arctic Ocean, certain seas, Antarctica, and the Australasian and Indonesian Islands, leading to reliance on atmospheric analysis estimates.

Many of the satellite systems that contributed data have been or will soon be replaced. Observation integrating models will be critical for ameliorating gaps and discontinuities in the data records caused by these transitions. Continued development of such models is essential for maximizing the value of remote sensing observations. Next generation observing systems are the best hope for significantly improving global water budget accounting.

1. Introduction

The most noticeable consequences of climate change will be impacts on the water cycle - water's journey through ocean, atmosphere, land, and back again - whose vagaries determine the distribution of humanity, agriculture, and all life on land, and also control circulation of the oceans and atmosphere. A robust, global inventory of current hydrologic flux rates is essential to the assessment and prediction of climate change. This hydrologic article and its energetic companion (L'Ecuyer et al., this issue) attempt to quantify the current state of the water and energy cycles, which is an important first step towards the NASA Energy and Water Cycle Study (NEWS) program goal of evaluating water and energy cycle consequences of climate change (NSIT, 2007). That is, in order to identify change, one must first establish the present condition. Our analysis also begins to address a grand challenge of the National Research Council's Decadal Survey in Earth Sciences, "to integrate in situ and space-borne observations to quantify the key water-cycle state variables and fluxes" towards identifying "large-scale and persistent shifts in precipitation and water availability" (NRC, 2007). This state of the water cycle assessment will serve as a baseline for hydroclimatic variability studies and climate change predictions and as a standard for Earth system model evaluations. By providing a rigorous accounting of errors, it also benchmarks the state of quantitative understanding of the water cycle and reveals the extent to which the water budget can be closed over multiple regions and timeframes given current observational capabilities.

Scores of global water cycle analyses have been performed over the past century, but several aspects make this one unique. First, it focuses on conditions during roughly the first decade of the 21st century, while previous analyses have made use of earlier data records and often stopped near the turn of century. Second, it makes use of the most modern data products, integrating data from satellite remote sensing as well as conventional observing systems. The 2000s have been rich with remotely sensed Earth observations that are relevant to the water and energy cycles. Third, rigorous assessments of uncertainty in the data products were supplied by the diverse group of data providers who compose the study team, and were examined and refined during the analysis. Fourth, an optimization algorithm was employed to compute the final water flux estimates, making use of the uncertainty assessments and constraining water balance on multiple scales: monthly, annual, continental, ocean basin, and global. Finally, the water and energy budgets were used to constrain each other through the equivalency of the evapotranspiration and latent heat flux terms, thus ensuring consistency between the two analyses.

In the following sections we describe the present state of knowledge of the global water cycle and results of this new analysis. Section 2 summarizes advances made by previous studies. Sections 3 and 4 detail the datasets and methods used herein. Section 5 presents water cycle fluxes during approximately 2000-2010, as monthly and annual means over six continents and nine ocean basins, as well as the global ocean and global land. Section 6 discusses implications and limitations of the results, and recommends future work.

2. Background

Characterizing the stocks and fluxes of Earth's global water budget has posed considerable challenges through the decades. In spite of the importance of water to humanity, ecology, and environment, a comprehensive global hydrological observing system for monitoring the storage and movement of Earth's water does not exist. Consequently, the earliest compilations (e.g., Bruckner, 1905; Nace, 1969; Korzoun, 1974) relied on limited observations to estimate globally-averaged fluxes of precipitation and evapotranspiration. Results varied widely (see, e.g., Schlosser and Houser, 2007) and have not enabled water budget closure (Chahine, 1992). Moreover, global water stocks such as groundwater were estimated using ad hoc assumptions for land properties, for example, aquifer thickness and porosity (Nace, 1964; Korzoun, 1974), yielding only first-order approximations of the magnitude of this and other critical reservoirs. Although such estimates should be used with caution, they have nevertheless been propagated in the literature, and continue to appear in modern global hydrological budgets and assessments (e.g. Shiklomonov, 1993; Oki and Kanae, 2006; Trenberth et al., 2007; 2011).

L'vovitch (1974), Baumgartner and Reichel (1975), Berner and Berner (1987) and others continued and updated global compilations, producing global maps as well as globally-averaged fluxes. Sparse ground-based data and simple water budget analyses were used to estimate spatial patterns of precipitation and evapotranspiration respectively. Because long-term measurements of river discharge are also limited in availability (Alsdorf et al., 2007), it is generally estimated as the difference of precipitation minus evapotranspiration in the above-mentioned studies, based on assumptions of negligible long-term net water storage change. Given current capabilities to observe terrestrial water storage changes using the NASA Gravity Recovery and Climate Experiment (GRACE) mission (Tapley et al., 2004; Wahr et al., 2004), such an assumption is no longer required, nor is it necessarily valid (Rodell et al., 2004a; Syed et al., 2010).

The evolution of the representation of the land surface in climate models (Dickinson et al., 1984; Sellers et al., 1986), and of large-scale hydrological models (Vörösmarty et al., 1989; Dirmeyer et al., 2006), has fostered a new generation of global water budget studies that supplement traditionally sparse hydrologic observations with global model output. Model output may itself be calibrated to (e.g., Dai et al., 2009), or otherwise constrained by observations (e.g.

Fekete et al., 2002), or may incorporate observations as input (e.g., Mitchell et al., 2004) or via data assimilation (e.g., Kumar et al., 2008). In lieu of sufficiently-dense hydrological observing networks, combined model-observational global budgets offer a physically-based alternative for producing well-constrained global water budgets. Oki and Kanae (2006), Trenberth et al. (2007), and Schlosser and Houser (2007) all provide recent examples.

Chahine (1992) ushered in the modern era of global water budget analyses, by providing insight that continues to help define the current research agenda. For example, Chahine (1992) was the first to articulate that water vapor, clouds and radiation, and sea surface fluxes are all major branches of the global water cycle, along with precipitation and terrestrial hydrology. Further, Chahine (1992) highlighted current inabilities to close the global water budget, and speculated that satellite remote sensing and integrative programs like the Global Energy and Water Cycle Experiment (GEWEX) may ultimately play a critical role in alleviating current shortcomings.

Clearly, both GEWEX and satellite remote sensing are contributing to global water budget analyses, as anticipated by Chahine (1992). Key contributions from the GEWEX program include the development of important research datasets (for example, the Global Precipitation Climatology Project [GPCP] for combining gauge and satellite based data to estimate global precipitation patterns; Huffman et al., 1997); the development of focused water cycle research questions to encourage community research; and integrative observing and modeling activities (GEWEX, 2012a,b). Meanwhile, the NEWS program has fostered the development of several satellite-based global hydrological datasets and combined model-satellite products, which contribute to the present study (see Section 3).

While tremendous progress has been made in global water budget analyses in recent years, several important issues remain unresolved. Differences among flux datasets still pose challenges for water budget closure, and by extension, for energy budget closure as well. Several key hydrologic stores and fluxes remain poorly measured in many regions of the world, for example, groundwater and surface water storage (Famiglietti and Rodell, 2013). The development of data assimilating modeling systems like the Land Information System (Kumar et al., 2008) are progressing rapidly, but they are not yet able to ingest, simultaneously, the full suite of data from water cycle observing satellites, including observations of surface waters, soil moisture, snow and vegetation properties, and terrestrial water storage.

The study described here addresses some of the aforementioned problems and leaves others for future work. By using predominantly satellite-derived datasets, data scarcity and accessibility issues are circumvented. By incorporating GRACE data on terrestrial or ocean water storage changes, water balance can be achieved at multiple scales (Rodell et al., 2004a; Syed et al., 2010). When model output is included in the analyses, it has been constrained by in situ or remote observations. In short, to our knowledge, the work presented here represents the most consistent, observation-based analysis of the global water budget that has been reported to date.

3. Data

The scales of this research are continental and major sea/ocean basin to global, and mean monthly to mean annual, during the period 2000-2010, though in some cases it was necessary to use data from as far back as 1998. Observation-integrating data products are favored, particularly those that incorporate satellite based measurements (Table 1). These criteria disqualify many of the datasets that are commonly used in hydroclimatological analyses. Further, we give preference to datasets provided by members of the NEWS team, which are generally the most modern available, over outside alternatives, because that ensures detailed understanding and well-vetted uncertainty assessments. While alternative datasets of similar quality certainly exist, we contend that none could definitively be described as better. In some cases, flux estimates from multiple sources are combined. In other cases, only one dataset is available, or one is chosen based on acceptance in the community as the standard. We are not anointing any of the chosen datasets as "best" and our choices should not be interpreted as a dismissal of others. Rather, the associated errors speak to the quality of each dataset, and it will be shown that the results of the water balance optimization suggest that both the choices of datasets and the associated error estimates are appropriate.

a. Precipitation

The Global Precipitation Climatology Project (GPCP) monthly Satellite-Gauge precipitation analysis (Adler et al., 2003; Huffman, et al., 2009), version 2.2, is the exclusive precipitation dataset used herein. It is a globally complete, monthly estimate of surface precipitation at 2.5° x 2.5° latitude–longitude resolution that begins in 1979, though this study made use of the period January 2001 to December 2010. The product employs precipitation estimates from the 6:00 am and 6:00 pm (local time) low-orbit satellite Special Sensor Microwave/Imager (SSMI) and Special Sensor Microwave/Imager and Sounder (SSMIS) microwave data to perform a calibration, that varies by month and location, of Geostationary Operational Environmental Satellite (GOES) infrared (IR) data in the latitude band 40°N-S. At higher latitudes, estimates based on Television Infrared Observation Satellite (TIROS)

Operational Vertical Sounder (TOVS) or Atmospheric Infrared Sounder (AIRS), calibrated by gauges over land and microwave estimates over ocean at lower latitudes, are combined with the SSMI and SSMIS microwave estimates to provide globally complete and homogeneous satellite-only precipitation estimates. These multi-satellite estimates are combined with rain-gauge analyses (over land) in a two-step process that adjusts the satellite estimates to the large-scale bias of the gauges and then combines the adjusted satellite and gauge fields with weighting by inverse error variance. Absolute magnitudes are considered reliable and inter-annual changes are robust. Precipitation may be underestimated in mountainous areas, although version 2.2 is improved in this regard over previous versions. Regional and global bias errors in the GPCP climatology have been estimated using data from other satellites, including the Tropical Rainfall Measuring Mission (TRMM), following Adler et al. (2012).

b. Ocean Evaporation

SeaFlux version 1.0 (Clayson et al., 2014) is our exclusive source of ocean evaporation data. SeaFlux is a satellite-derived surface turbulent flux dataset currently produced at 0.25° spatial resolution and 3-hourly temporal resolution. While many other satellite based products are produced at coarser resolution through binning, averaging, and statistical interpolation, SeaFlux attempts to utilize the high-resolution nature of the satellite data. It includes a sea surface temperature dataset with diurnal warming specifically included (Clayson et al., 2014). The bulk atmospheric parameters of temperature and humidity are provided by SSMI retrievals using a newly-developed neural net algorithm (Roberts et al. 2010). This retrieval method reduces both mean biases in comparisons with in situ data and also systematic errors at extremely low and high humidity. Air temperature retrievals using this method have shown the greatest increase in accuracy compared to other products, with biases now under 0.25º C across the spectrum of air-sea temperature differences. Winds are provided by the Cross-Calibrated Multi-Platform (CCMP) level 2.5 gridded swath product. A novel interpolation method based on the use of the temporal evolution of a model-reanalysis (for SeaFlux v.1, NASA's Modern Era Retrospective-analysis for Research and Applications [MERRA; see section 3.3b] is the reanalysis used as the basis) has been implemented. This reanalysis-based interpolation uses the time tendencies from a high-resolution model analysis but is driven through the satellite observations in a smooth manner. The interpolation algorithm selectively takes the physically-calculated time tendencies from the model results to interpolate the missing data points at a 3 hourly resolution. A neural network emulation of the Coupled Ocean-Atmosphere Response Experiment (COARE) 3.0 algorithm (Fairall et al., 2003) has been developed as a computationally inexpensive forward model to calculate the surface turbulent fluxes from the input bulk variables. The version of the SeaFlux product used here covers 1998-2007 and integrates the Colorado State University SSMI calibrated brightness temperature dataset (C. Kummerow, personal communication, 2011).

c. Terrestrial Evapotranspiration

Estimating evapotranspiration (ET) at large scales is challenging because ET is highly variable in space and time, and weighing lysimeters, which are the gold standard, are difficult and expensive to install and maintain. More commonly, ground based observation is accomplished using eddy covariance measurements. While satellite retrieval algorithms do exist, their accuracy is limited by the sparseness of in situ observations available for calibration and validation, which themselves may be unrepresentative of 500 m and larger scale satellite footprints and grid pixels. Other alternatives include physically based and empirical models of land surface processes, which are limited in accuracy by the quality of the input data and the simplifications inherent to numerical models, and river basin scale water budget analysis (e.g., Rodell et al., 2004a), which requires river discharge data and is best suited for large river basins.

Due to these challenges and the resulting uncertainty in any one technique, ET estimates from three sources are averaged to produce the values used herein. Total uncertainty (bias and random errors) in the averaged values is estimated as the standard deviation of the three estimates for each region and time period. The three sources are Princeton University's remote sensing-informed Penman-Monteith scheme and NASA's MERRA and Global Land Data Assimilation System (GLDAS).

1) Princeton Remote Sensing Based ET

Princeton's model for global ET estimation (Vinukollu et al., 2011) is based on the Penman–Monteith approach (Monteith, 1965). All model inputs and forcings, with the exception of wind and surface pressure, are derived from satellite remote sensors including AIRS, the Moderate Resolution Imaging Spectroradiometer (MODIS), the Clouds and the Earth's Radiant Energy System (CERES), and the Advanced Very High Resolution Radiometer (AVHRR). Surface resistance is adjusted and ecophysiological constraints are applied to account for changing environmental factors. Evaporation and sublimation over snow-covered regions is calculated using a modified Penman equation. Instantaneous fluxes of latent heat computed at the time of satellite overpass are linearly scaled to the equivalent daily evapotranspiration using the computed evaporative fraction and the day-time net radiation. A constant fraction (10% of daytime evaporation) is used to account for the night-time evaporation. Interception losses are computed using a simple water budget model. Satellite-based inputs and model outputs are first carefully evaluated at the site scale on a monthly-mean basis, then as a multi-year mean against a climatological estimate of ET over 26 major basins, and finally in terms of a latitudinal profile on an annual basis. Input meteorology and resulting latent and sensible heat fluxes have been evaluated against eddy-covariance tower data across the U.S. These exercises revealed good correlations with the in situ data and proper representation of seasonal cycles and major droughts.

2) MERRA

MERRA (Rienecker et al. 2011) has reanalyzed the recent satellite era (1979-present) utilizing a significant portion of the available in situ and satellite data records, including those from GOES and European Remote Sensing Satellites 1 & 2 (ERS1/2) instruments, AIRS, SSMI, MODIS, Microwave Sounding Unit (MSU) and Advanced Microwave Sounding Unit (AMSU), Stratospheric Sounding Unit (SSU), High resolution Infrared Radiation Sounder (HIRS), and Quick Scatterometer (QuikSCAT). NASA's Goddard Earth Observing System Model, Version 5 (GEOS-5; Rienecker et al., 2008) is the model basis. MERRA water and energy budget data are reported hourly on a nominal 0.5° grid. In the development of the output diagnostics, special care was taken to include all the budget terms so that budget closure could be achieved. Of course, like all reanalyses, the observational analysis exerts significant influence on the physics budgets (e.g., Roads et al. 2002) which leads to imbalances in the physical terms of the budget. In MERRA, this influence is computed from the data assimilation and provided as a tendency term (called the analysis increment) in the budget equation, so that it does not need to be derived from residuals. The analysis increments generally reflect the long term bias present in the background model. In this study, we use MERRA data that are averaged over 1998-2009. We have corrected the precipitation, evapotranspiration, and runoff fields to account for the analysis increments, using regression equations based on Bosilovich and Schubert (2001). Bosilovich et al. (2011) discuss the strengths and weaknesses of the MERRA global water and energy budgets, including the interrelationships of the physical terms with the analysis increment. Despite the strengths and utility of the MERRA dataset, Trenberth et al. (2011) caution that there are land regions over which atmospheric convergence is negative. Further, the satellite data assimilated by MERRA (Table 1) have only an indirect influence on ET through their effects on air temperature, specific humidity, and wind velocity.

A supplemental land surface reanalysis, MERRA-Land, provides enhanced land surface hydrology estimates based on a land-only GEOS-5 simulation (Reichle et al., 2011; Reichle, 2012). Compared with MERRA, MERRA-Land claims two advantages. First, the version of the land surface model within GEOS-5 has been updated from that used in MERRA. Second, precipitation forcing fields from MERRA are corrected with the global, gauge-based NOAA Climate Prediction Center "Unified" (CPCU) precipitation product (Chen et al., 2008). In this analysis, the mean of MERRA and MERRA-Land ET is used as the “MERRA ET estimate”, which is subsequently averaged together with the Princeton and GLDAS ET estimates.

3) GLDAS

GLDAS (Rodell et al., 2004b) is a quasi-operational implementation of the Land Information System software (Kumar et al., 2008), which drives multiple land surface models (LSMs) and offers numerous options of input parameter and meteorological forcing datasets, spatial scales, and other functionalities. The goal of GLDAS is to generate optimal fields of land surface states (e.g., soil moisture, temperature) and fluxes (e.g., evapotranspiration, runoff) by integrating satellite- and ground-based observational data products within a suite of LSMs. The

GLDAS output fields have been evaluated in a variety of studies through comparison with observations and other model products, and in general they compare favorably, particularly when the multi-model GLDAS mean is used (Kato et al., 2007; Syed et al., 2008; Zaitchik et al., 2010; Jimenez et al., 2011; Mueller et al., 2011; Wang et al., 2011). This study utilizes 1.0° resolution output from GLDAS instances of the Noah (Chen et al., 1996; Ek et al., 2003; Koren et al., 1999), Community Land Model (CLM) version 2 (Bonan et al., 2002), Variable Infiltration Capacity (VIC; Liang et al., 1994), and Mosaic (Koster and Suarez, 1996) LSMs. The models were forced with a combination of meteorological fields (air temperature, humidity, wind speed, and surface pressure) from the National Centers for Environmental Prediction (NCEP) Global Data Assimilation System product, precipitation fields from the GPCP One-Degree Daily (1DD) product version 1.1 (Huffman et al., 2001), and downward shortwave and longwave radiation fields derived from Air Force Weather Agency cloud analyses using the schemes of Shapiro (1987), Idso (1981), and Wachtmann (1975). The GPCP 1DD data were downscaled to 3-hourly resolution by bias correcting precipitation fields from MERRA for 1998-1999 and from GDAS for 2000-2009. All four models were parameterized with land cover data from the University of Maryland (Hansen et al., 2000), soils data from Reynolds et al. (2000), and the GTOPO30 digital elevation model (available from http://eros.usgs.gov/#/Find_Data/Products_and_Data_Available/gtopo30_info). The GLDAS simulations were previously spun up from 1979 and were executed on 15-minute time steps (except for VIC, whose time step is 1-hour). A GLDAS climatology is constructed by averaging the four models over the period 1998-2008 (due to the current unavailability of GPCP 1DD data after mid-2009) to produce monthly means. Inland water bodies (e.g., the Great Lakes) and ice sheets (Greenland and Antarctica) not modeled by GLDAS are filled with MERRA data in order to conform to the continental delineation defined for this study.

d. Continental Runoff

Clark et al. (2014) estimated river runoff using a method, similar to that of Dai et al. (2009), that combined gauged streamflow from 839 near-coast gauging stations and simulated runoff from two implementations of the VIC model. The first VIC simulation (SHEFF), for the period of 1949-2008, was performed at 1° resolution in full energy balance mode (energy balance calculations performed at each hourly time step) forced with the surface meteorological inputs of Sheffield et al. (2009). The second (WATCH), from 1959-2001, was run at 0.5° resolution in VIC water balance mode (energy budget balanced daily) forced with surface meteorological inputs from the European Union's Water and Global Change programme (EU-WATCH; Weedon et al., 2011). Simulated gauge and river mouth streamflow was calculated by routing these runoff values through the STN-30p v6.01 flow network (Vörösmarty et al., 2000). Gaps in the gauge records were filled through linear regression of monthly or annual gauged streamflow against simulated streamflow. Gauged flows were extrapolated at monthly and annual time steps to river mouths based on the ratio of simulated runoff at the mouth to simulated runoff at the station. Flows at the mouths of completely ungauged rivers were estimated by multiplying simulated flow at that river mouth with the ratio of observed to simulated flows for all gauged rivers within +/-2° latitude of that mouth. The latitude bands included either all stations +/-2° latitude on the same continent (CONT) or draining to the same ocean (OCN).

The annual and monthly runoff estimates used here are the average of SHEFF-CONT and SHEFF-OCN from 1999-2008. Because this approach assumes that the model performance is regionally consistent and that some of the residual errors are averaged out in the aggregate, neither of which can be easily tested with existing data, we estimated errors based on multiple data sets. Errors in annual and monthly runoff are estimated as the standard deviation of estimates from the SHEFF-CONT (1998-2008), SHEFF-OCN (1998-2008), WATCH-CONT (1960-2001), WATCH-OCN (1960-2001), Dai et al. (2009)'s estimate (1998-2004), GLDAS simulated runoff, and MERRA simulated runoff.

Over Greenland and Antarctica, observations of runoff (which consists primarily of ice flows) are not available. Therefore monthly runoff is computed as a water budget residual.

In order to account for total continental runoff, submarine groundwater discharge (SGD) must be added to river runoff. Many localized estimates of SGD are available, but these are not easily scaled up, and directly comparable continental SGD estimates have not been published, to our knowledge. Korzun (1974) estimated global SGD to be 2,200 km^3/yr, while Zektser et al. (2006) estimated 2,200-2,400 km^3/yr. Here we take the midpoint of the latter range, 2,300 km^3/yr, and distribute it among the continents by assuming that SGD is proportional to both surface runoff and coastline length. The "coastline paradox" is the observation that, due to the fractal nature of coastline features, estimated coastline length increases with the precision of one's measurements (Mandelbrot, 1983). Because we are concerned only with the relative lengths of continental coastlines at macro scales, and because small-scale features such as fjords are unlikely to increase large-scale SGD relative to that of a flat coastline, we estimate continental coastline length based on a 0.25° resolution gridded map (Table 2). We then use the product of continental coastline length and mean annual continental river runoff to weight the distribution of the 2,300 km^3/yr SGD among the continents. Monthly SGD is computed by assuming it is directly proportional to monthly river runoff, and the results are added to the monthly river runoff values to estimate total monthly, continental runoff. Despite the vast majority of Antarctic surface runoff being frozen, in the form of glacier calving into the ocean, Antarctic SGD has indeed been measured (Uemura et al., 2011), explained by the combination of geothermal heating and pressure which produces liquid water lakes beneath the ice sheet. Owing to the scarcity of large scale SGD estimates and our reliance on several simplifying assumptions, uncertainty in our estimates is conservatively computed as 50% of SGD itself.

e. Atmospheric Convergence

Atmospheric convergence data are taken from three sources. The first is MERRA, which has full global coverage. The second source is a water vapor transport product developed by Liu et al. (2006). It is based on an accounting of moisture fluxes over the continental margins derived from QuikSCAT data, constrained by rainfall from TRMM, terrestrial water storage changes from GRACE, and climatological river discharge. This product is available on a monthly basis over the major ocean basins, but over land it is limited to two continents, North and South America, as annual averages. The third source is the Passive Microwave Water Cycle (PMWC) dataset (Hilburn, 2009). PMWC version 2.0 was constructed using retrievals of wind speed, water vapor, and rain rate from Remote Sensing Systems (RSS) intercalibrated data record of the Advanced Microwave Scanning Radiometer for EOS (AMSR-E; Kawanishi et al., 2003), AMSR2, SSMI, SSMIS, TRMM Microwave Imager (TMI), and WindSat. PMWC derives water vapor transport from the satellite water vapor data using MERRA to specify the effective transport velocity. PMWC estimates are only available over the major ocean basins.

Over the ocean basins all three products are combined by simple averaging. For the North and South American annual means, the MERRA and the QuikSCAT estimates are averaged. For the monthly means and for all other continents MERRA alone is used due to large uncertainties in the QuikSCAT estimates. In cases where multiple estimates are available, monthly and annual errors are estimated as the standard deviation of the available estimates, but not less than 3 mm/month. In cases where only the MERRA estimate is available (the Arctic Ocean, the Caribbean, Mediterranean, and Black Seas, and continents other than the Americas), the error is fixed at 19% (the error percentage computed for South American annual convergence) or 3 mm/month, whichever is larger.

f. Terrestrial and Oceanic Water Storage Changes

Monthly changes in terrestrial water storage (TWS) for each continent and the global ocean have been derived from GRACE satellite observations of Earth's time-varying gravity field (Tapley et al., 2004). The gravity coefficients used here are from the University of Texas Center for Space Research's Release-05 product (Bettadpur, 2012), for 2003 to 2012. They were processed with standard corrections to account for the degree 2, order 0 coefficients, geocenter motion, and glacial isostatic adjustment (Chambers and Schröter, 2011; Chambers and Bonin, 2012). Average continental water storage was computed using the method of averaging kernels convolved with the GRACE coefficients, with results scaled based on convolutions with simulated data in order to restore power of the signal reduced by the resolution of GRACE (Swenson and Wahr, 2002). The kernels and scaling factors for the continents have previously been described and tested (Chambers, 2009; Johnson and Chambers, 2013). Formal GRACE "instrument errors" account for random GRACE errors, gravity signals outside the area of interest leaking into the estimate, and the variance of intra-annual variations. TWS as observed by GRACE comprises all water in and on the land, including groundwater, soil moisture, surface water, snow and ice, and biological water. This definition is precisely appropriate for the terrestrial water budget equation (see section 4.3). However, GRACE provides monthly mean anomalies of TWS, which cannot be used directly to compute the change in TWS between the start and the end of a given month as required by the standard terrestrial water budget (equation 6 in section 4.3; see Rodell et al., 2004a). Thus daily TWS changes are estimated here by linearly interpolating the GRACE data and then applying a scale factor so that the interpolated daily values approximately average to the observed monthly values. Changes in TWS between the first days of adjacent months are then computed.

Monthly changes in world ocean water volume have likewise been estimated based on GRACE data (Johnson and Chambers, 2013). Changes in water volumes of individual ocean basins are not included in the analysis owing to a lack of ocean transport data to balance the ocean basin water budget. Total uncertainty in the GRACE-based TWS changes for each continent and the global ocean is estimated as the root sum square of three error components: formal instrument errors, atmospheric errors, and leakage errors. That result is then multiplied by the square root of two in order to account for uncorrelated errors in the two consecutive months used to compute a change (Wahr et al., 1998; Rodell and Famiglietti, 1999; Landerer and Swenson, 2012).

g. Total Precipitable Water Vapor

Total precipitable water vapor have been derived from AIRS and AMSR-E observations from the NASA Aqua satellite. The AIRS spectral resolution is 100 times greater than previous infrared sounders, revealing detailed three-dimensional global distribution of water vapor (e.g. Gordon et al., 2014; Tian et al., 2013). The AIRS water vapor is based on a physical relaxation algorithm (Susskind et al., 2011). AMSR-E is a twelve-channel, six-frequency, passive microwave radiometer system, which can provide precipitable water vapor measurements over water only, where low surface emissivity provides a low temperature background for retrieval of atmospheric properties. The AMSR-E retrieval uses a regression against operational radiosondes, with updated validation against a separate subset of radiosondes (Wentz and Meissner, 2000).

AMSR-E total water vapor data have negligible biases and RMS differences of about 6% absolute compared with radiosondes (Szczodrak et al., 2006; see Fetzer et al., 2006 for a discussion). The AIRS and AMSR-E total water vapor estimates were shown by Fetzer et al. (2006) to have relative biases of 5% or less (though of undetermined sign) and RMS difference of 10% or less for clear or partly cloudy scenes, while AIRS-AMSR-E relative biases ranged from -30% (AIRS dry) to +70% for persistently cloudy conditions. AIRS total water vapor over land and ocean has been validated against radiosondes (Tobin et al., 2006; Divakarla et al., 2006), Global Positioning System receivers (Rama Varma Raja et al., 2008), and group-based radiometers (Bedka et al., 2010). Using a seven-year surface record at three fixed sites, Bedka et al. (2010) reported monthly mean total water vapor biases of 1-3% for a wide range of weather conditions and total water vapor amounts, showing that the cloud-induced sampling in AIRS is generally small. However, the AIRS sampling biases are largest in regions of deep convection and baroclinic activity. The global implications of these cloud-induced biases are discussed by Tian et al. (2012; 2013), Hearty et al. (2014) and Yue et al. (2013). AMSR-E water vapor sampling biases are small except under heavily precipitating conditions representing 2-5% of all scenes.

Here we utilize the AIRS and AMSR-E Version 5 Level 2 (vector) 3-hourly total precipitable water vapor at 1-degree from 2003 to 2007. To compute a climatology of monthly atmospheric moisture storage changes over the continents and ocean basins, the vector data are first binned into 1° grids, and then time series of 5-day averages centered on the first day of each month are generated to achieve global coverage with minimal data gaps. Smaller RMS uncertainties are expected for the averaged data used in this analysis because they typically represent 10 to 20 samples, each with RMS error of 10% or less. Biases of the 5-day averages are estimated to be 5% or smaller, consistent with Bedka et al. (2010).

4. Methods

a. Data Blending

As described above, in many cases a single data source is chosen, with other sources used for corroboration. When multiple datasets meet the criteria and selecting only one is not defensible, a single estimate of a given water budget variable is computed by averaging. The standard deviation across the original estimates is then taken to represent the uncertainty in the blended estimate. Typically this results in an uncertainty value that is similar to or more conservative (larger) than the original uncertainties. Blended estimates are computed for terrestrial evapotranspiration, atmospheric convergence over the major ocean basins and North and South America, and total precipitable water vapor changes over the ocean.

b. Water Budget Equations

This section presents the water budget equations that are applied at each spatial and temporal scale and used with the optimization approach described above. A capital "A" in the equation number indicates that the equation only applies to the long term annual mean, assuming no climate or human induced change in the water cycle. For any variable *X* (flux or change in storage with units of mass over time) over any area, the annual total must equal the sum of the monthly fluxes or changes,

$$X_{Annual} = X_{January} + X_{February} + \dots + X_{December} \qquad (1)$$

and over any time period, the worldwide total must equal the sum of the global land and global ocean fluxes or changes,

$$X_W = X_L + X_O \qquad (2)$$

where the subscripts W, L, and O represent world, land, and ocean.

At the continental scale, the surface terrestrial water budget equation is

$$\mathrm{dS_{co} = P_{co} - ET_{co} - Q_{co}} \qquad (3)$$

where dS is the change in storage between to two distinct points in time, P, ET, and Q are total precipitation, evapotranspiration, and runoff in the interval, and the subscript *co* denotes continental. On an annual mean basis, assuming no changes in climate or direct human impacts on water storage, $\mathrm{dS_{co}}$ drops to zero, so that

$$P_{co} - ET_{co} = Q_{co} \qquad (3A)$$

The atmospheric water budget over a continent is

$$dW_{co} = C_{co} - P_{co} + ET_{co} \qquad (4)$$

where dW is the change in precipitable water in the atmospheric column, and C is net atmospheric convergence. The change in liquid water in the column, which is sometimes included on the left side of equation (4), was assumed to be negligible (Peixoto and Oort, 1992). On an annual mean basis dW_{co} becomes zero, so that

$$C_{co} = P_{co} - ET_{co} \qquad (4A)$$

It follows from (3) and (4) that

$$dS_{co} + dW_{co} = C_{co} - Q_{co} \qquad (5)$$

and on an annual mean basis

$$C_{co} = Q_{co} \qquad (5A)$$

The ocean basin water budget equation is

$$dS_{ob} = P_{ob} - E_{ob} + Q_{ob} + T_{ob} \quad (6)$$

where E is ocean evaporation, Q_{ob} is runoff from the continents into the ocean basin, and T_{ob} is net transport of water into an ocean basin (*ob*). As before, the storage term drops to zero on an annual mean basis, leaving

$$E_{ob} = P_{ob} + Q_{ob} + T_{ob} \quad (6A)$$

Because observation-based estimates of T are not available, equations (6) and (6A) are not included in the analysis. The atmospheric water budget over an ocean basin is identical to that over a continent except that ET is replaced by E,

$$dW_{ob} = C_{ob} - P_{ob} + E_{ob} \quad (7)$$

and on a mean annual basis,

$$C_{ob} = P_{ob} - E_{ob} \quad (7A)$$

For the sake of completeness, we note that following (6) and (7),

$$dS_{ob} + dW_{ob} = C_{ob} + Q_{ob} + T_{ob} \quad (8)$$

and on a mean annual basis

$$C_{ob} = -Q_{ob} - T_{ob} \tag{8A}$$

For the global land and oceans, water storage changes must balance as

$$dS_L + dS_O = -dW_L - dW_O \tag{9}$$

which, based on (2), is identical to

$$dS_W = -dW_W \tag{9b}$$

with all of these terms dropping to zero on a mean annual basis. The net movement of water vapor over the land is a net loss from the atmosphere over the oceans, so that

$$C_L = -C_O \tag{10}$$

and C_W must be zero. Similarly, here we define

$$Q_O = Q_L \tag{11}$$

though some may prefer to define one as the additive inverse of the other, and adjust (6) and (8) accordingly. The other lateral transport, T, has no meaning at the global ocean scale. Thus, from (6), the global ocean water budget is

$$dS_O = P_O - E_O + Q_O \tag{12}$$

and for the annual mean,

$$E_O = P_O + Q_O \tag{12A}$$

The budget equation for the global ocean-atmosphere column then follows from (8),

$$dS_O + dW_O = C_O + Q_L \tag{13}$$

Similarly, the budget for the global land-atmosphere column is unchanged from (5),

$$dS_L + dW_L = C_L - Q_L \tag{14}$$

and on an annual basis,

$$C_L = Q_L \tag{14A}$$

Finally, by combing equations, it can be shown that

$$dS_W = P_W - E_W \quad (15)$$

and on an annual basis,

$$E_W = P_W \quad (15A)$$

c. Water Budget Closure

Taken individually, the observed fluxes described in the section 3 represent our best estimates of those terms, irrespective of the observational uncertainty. On the other hand, the fluxes (and associated storage terms) are related to one another by the water budget equations described in subsection 4.2. These budget equations therefore provide additional information that can be used to modify the observed fluxes and storage terms to obtain “optimized” fluxes and storage terms that balance all relevant budget equations while remaining consistent with the observations and their associated uncertainties. Further, it is desirable to achieve simultaneous water and energy budget closure (via the equivalence of evapotranspiration and latent heat flux), addressing all available global and regional budget constraints. Applying concepts from the variational data assimilation and optimal estimation retrieval communities demonstrated in L’Ecuyer and Stephens (2002), we employ a new objective approach for adjusting all component fluxes that explicitly accounts for the relative accuracies to which they are known. The annual and monthly observational flux estimates are modified according to the optimization method that follows.

Suppose we have a set of N flux terms that are represented by

$$\boldsymbol{F} = (F_1 , F_2 , F_3 , \ldots , F_i, \ldots , F_N)^T, \tag{16}$$

(T denotes transpose, i.e., $\boldsymbol{F}$ is a column vector) and that these fluxes are related to storage terms by budget equations that can be written, in general,

$$\boldsymbol{R} = \boldsymbol{A} \boldsymbol{F} , \tag{17}$$

where $\boldsymbol{R}$ is the vector of M water storage residuals and $\boldsymbol{A}$ is the matrix representing the budget equations. For the j^{th} water storage residual,

$$R_j = \sum_{i=1}^{N} a_{ji} \; F_i , \tag{18}$$

where each a_{ji} is an element of $\boldsymbol{A}$. Then, optimization of the fluxes F_i demands minimizing the functional

$$J \equiv (\boldsymbol{F} - \boldsymbol{F_{obs}})^T \boldsymbol{S_{Fobs}^{-1}} (\boldsymbol{F} - \boldsymbol{F_{obs}}) + (\boldsymbol{R} - \boldsymbol{R_{obs}})^T \boldsymbol{S_{Robs}^{-1}} (\boldsymbol{R} - \boldsymbol{R_{obs}}) , \tag{19}$$

where $\boldsymbol{S_{Fobs}}$ and $\boldsymbol{S_{Robs}}$ are covariance matrices representing the uncertainties of $\boldsymbol{F_{obs}}$ and $\boldsymbol{R_{obs}}$, respectively. Here, ***obs*** denotes an observed flux/storage, and the unsubscripted flux/storage terms represent optimized values. Minimizing J with respect to $\boldsymbol{F}$ gives (e.g., Rodgers, 2000)

$$\boldsymbol{F} = \boldsymbol{F_{obs}} + \left(\boldsymbol{K^T S_{Robs}^{-1} K} + \boldsymbol{S_{Fobs}^{-1}}\right)^{-1} \boldsymbol{K^T S_{Robs}^{-1}} \left(\boldsymbol{R_{obs}} - \boldsymbol{K F_{obs}}\right), \tag{20}$$

where $\boldsymbol{K}$ is the Jacobian of $\boldsymbol{R}$ with respect to $\boldsymbol{F}$. The solution for the optimal $\boldsymbol{F}$ is otherwise known as the maximum *a posteriori* solution, and the uncertainty of this solution is given by the error covariance,

$$\boldsymbol{S_F} = \left(\boldsymbol{K^T S_{Robs}^{-1} K} + \boldsymbol{S_{Fobs}^{-1}}\right)^{-1}. \tag{21}$$

Due to lack of information regarding the correlation of the errors of different fluxes/storage terms, all off-diagonal covariance elements of $\boldsymbol{S_{Fobs}}$ and $\boldsymbol{S_{Robs}}$ are assumed to be zero. Also, in many cases it is assumed that the water fluxes exactly offset one another in a given budget equation (e.g., the annual equations labeled with an "A" in section 4.2), and in these cases, $R_j = 0$, and a small uncertainty ($\leq$ 0.016 mm/day) is assigned to the corresponding error variance in $\boldsymbol{S_{Robs}}$. In these cases, stable solutions are found for $\boldsymbol{F}$ that are consistent with $\boldsymbol{F_{obs}}$ and their uncertainties while obeying the specified budget equation with no change in storage. Similarly, stable solutions are found when observations suggest R_j /= 0 (e.g., monthly surface and atmospheric water budget). Solutions may be unstable when the uncertainty is too small, so in those cases the uncertainty was raised until a reasonable solution was achieved by comparing the magnitude of the flux adjustments against their estimated uncertainties.

1) Annual Optimization

The foregoing optimization framework is first applied to the collection of observations on an annual mean basis. Taking advantage of the equivalence of evapotranspiration and latent heat flux, all water and energy fluxes are optimized simultaneously to achieve coherent water and energy budget closure. The fluxes that are optimized include the horizontal convergence of atmospheric water vapor, *C*, evapotranspiration, *E*, precipitation, *P*, runoff, *Q*, surface longwave downwelling radiation, *DLR*, surface shortwave downwelling radiation, *DSR*, surface longwave upwelling radiation, *ULW*, surface shortwave upwelling radiation, *USW*, and surface sensible heat flux, *SH*, over the seven continental regions and the global ocean. Also optimized are the global net outgoing longwave radiation, *OLR*, and the global net downwelling shortwave radiation, *TSR*, both at the top of the atmosphere. These annual mean fluxes are constrained by the budget equations that describe the annual storage of water vapor, *dW*, terrestrial water, *dS,* and downward transfer of energy at the earth's surface, *NET*, over the seven continental regions and the global ocean. Application of simultaneous closure in individual ocean basins is impossible without estimates of water and energy transport between adjacent basins. While technically feasible to constrain C, P, and E to *dW* at each basin in this framework, we find that it biases all results towards those flux estimates that are contained in the most equations within the optimization routine. In particular, including C, P, and E in twelve additional equations biases the results away from the energy flux estimates, simply because the latter are then represented in fewer equations than the water flux estimates. For this reason, all fluxes except for TSR and OLR are optimized through *dW*, *dS,* and *NET* constraints over the seven continental regions and the global ocean (i.e. sum of all basins), whereas TSR and OLF are constrained to the global NETA balance (i.e., sum of all regions). Observed annual *dW* for all regions are equal to or very close to zero as expected. It is assumed that *dS* is zero in all regions, although in reality trends in *S* do exist (e.g., Luthcke et al., 2013). Similarly, the net energy transfer to the earth, *NET*, over each land region is assumed to be zero, while the net energy transfer to the ocean basins is assumed to be 0.6 W m^{-2} with an uncertainty of 0.4 W m^{-2}, based upon recent estimates of ocean heat storage from the Argo array (Willis et al., 2009; Lyman et al., 2010). Regarding energy in the atmosphere, it is assumed that the global annual-mean net storage of energy is zero,

$$NETA = TSR - OLR + L_v P + SH - DLR - DSR + ULW + USW \ = 0\,, \tag{22}$$

and that the convergence of atmospheric dry static energy is zero on a global, annual-mean basis. The specific implementation of $\boldsymbol{F_{obs}}$ and $\boldsymbol{R}$ is presented in Appendix A and further discussed in the companion article by L'Ecuyer et al. (2014).

The resulting global ocean water component fluxes, C, E, and P, are in balance with the energy fluxes. Next we seek to adjust the water fluxes in each ocean basin so that they sum up to the optimized global ocean fluxes while maintaining the atmospheric water balance. First, the fluxes are optimized through the dW constraint at individual basins. Subsequently, a Lagrange multiplier approach (e.g., Bertsekas, 1996) is used to adjust the optimized basin fluxes according to the error variance of the individual basin fluxes. Here, we wish to obtain the spatially constrained basin fluxes, G_l, and the corresponding global ocean flux, F, such that

$$F \ = \ \frac{1}{L}\sum_{l=1}^{L} G_l\,, \tag{23}$$

where l is the index for basins 1 to L, with L=9. Because an exact match between the sum of basin fluxes and the global ocean flux is desired, a strong constraint approach is taken, and the Lagrangian to be minimized is

$$\Lambda = \sum_{l=1}^{L} \frac{(G_l - GO_l)^2}{2\,\sigma_l^2} + \lambda \left(F - \frac{1}{L} \sum_{l=1}^{L} G_l \right), \qquad (24)$$

where σ_l is the uncertainty of the l^{th} optimized basin flux, GO_l from the first step, and λ is a Lagrange multiplier. After taking the derivative of (24) with respect to λ, setting the result to zero, and substituting terms, the adjusted flux at k^{th} basin is obtained through the relationship,

$$G_k = GO_k + \frac{L\,\sigma_k^2}{\sum_{l=1}^{L} \sigma_l^2} \left(F - \frac{1}{L} \sum_{l=1}^{L} GO_l \right). \qquad (25)$$

2) Monthly Optimization

Annual optimization is performed first because the observed annual-mean fluxes and their uncertainties are deemed more reliable than the monthly fluxes. Changes in storage also must be accounted at sub-annual scales. Energy balance constraints are weakened due to the lack of reliable heat transport observations, so that only the monthly water fluxes are optimized within the same framework as that of the annual scale. With the water and energy budgets being decoupled, it is now desirable to enforce atmospheric water balance over each basin.

Monthly optimization is performed in two steps. Lacking a complete set of energy fluxes, the first step is to use the same set of budget equations as in the annual optimization but without any constraints on *NET* and *NETA*; i.e., only the *dW* and *dS* constraints are imposed. This first step is performed for all months separately; however, the resulting optimized monthly fluxes are not necessarily consistent with the optimized annual-mean values. Therefore, a second “hard” constraint step is applied to ensure that the sum of the monthly fluxes of each category are exactly equal to the optimized annual total flux, but respecting the relative uncertainty of each monthly observation. In the second step, a Lagrange multiplier approach is again used, this time to adjust the monthly fluxes derived from the first step, identified generically here as GO_l, where l is the index for a particular month. If the annually-constrained monthly fluxes are denoted by G_l, and the corresponding annual flux is denoted by F, as above, then the constraint on the adjusted fluxes is expressed as in (23), this time with $L = 12$ (note that the only purpose and effect of dividing by L is consistency of units, i.e., both F and G_l are quantified in cm/month in this application). The Lagrangian to be minimized is defined in (24), but in this case, σ_l is the uncertainty of the l^{th} optimized monthly flux, GO_l, and λ is a Lagrange multiplier. The solution for the k^{th} adjusted monthly flux is found using (25). Note that each monthly flux from the first step is adjusted based on the bias of the annual mean, in proportion to the uncertainty of that flux, and that the annual mean of the adjusted G_k is equal to F.

d. Metrics

Evaluation of an analysis and resulting dataset is difficult when most of the pertinent data are incorporated into the final product. Nevertheless we identify three metrics of success. First, the new global flux estimates are compared with those of Trenberth et al. (2011) and Oki and Kanae (2006), two recent, well regarded global water budget analyses. We presume that the latter should lie within the error bounds of our new estimates. Second, the initial and optimized uncertainty estimates are compared with residuals of the pre-optimization (observed) water budgets at multiple scales. A residual that was much larger than the estimated total uncertainty would suggest that uncertainty in one or more of the fluxes was overly optimistic (small). Third, the difference between the observed and optimized estimates of any variable should be smaller than the uncertainty in that variable, else the predicted uncertainty was overly optimistic.

5. Results

a. Mean Annual Fluxes

The mean annual fluxes of the global water cycle and associated uncertainty ranges are depicted in Figure 1. The white numbers are the original "observed" fluxes and uncertainties from either a single, preferred source or an average over multiple estimates. The blue numbers are the estimates resulting from water cycle closure using the optimization technique described in Section 4. Annual precipitation, evapotranspiration, and runoff over the global land surface are estimated to be 116,500 ±5,100, 70,600 ±5,000, and 45,900 ±4,400 km^3/yr, respectively, after optimization. Annual precipitation and evaporation over the global ocean surface are estimated to be 403,600 ±22,200 and 449,500 ±22,200 km^3/yr after optimization. For reference, the capacity of the Great Lakes is about 23,000 km^3 (Fuller et al., 1995), and mankind's global, annual water footprint related to agriculture, industry, and domestic water supply is about 9,100 km^3/yr (Hoekstra and Mekonnen, 2012), so the magnitudes of these freshwater fluxes are staggering. The optimization routine produces revised error estimates as a standard output. Narrowing of the uncertainty range is a natural statistical response to the application of new constraints, similar to increasing the sample size when computing an expected value. Whether or not the optimized values are in fact closer to the truth than the original observed estimates depends in part on the veracity of the assumption that those original estimates are unbiased.

In all cases the optimized global annual flux estimate is well within the uncertainty range of the observed estimate, save for ocean evaporation, which is just outside of the range. That bodes well for the realism and conservatism of the original error estimates. Further, the same is true for the observed fluxes and the optimized ranges, again with the exception of ocean evaporation. The large adjustment to ocean evaporation is due in part to simultaneous closure of the energy budget, and it is examined further in the Discussion section.

Overall, the compatibility (in the sense of a closed water budget) of the observed water cycle fluxes, which are largely but not completely independent in their origins, is encouraging. The observed global, annual, terrestrial water budget (equation 6A applied to all land) closes with a residual equal to 4.3% of P_L, considerably better than the expected error of 10.1% (computed as the square root of the sum of the squares of the component flux errors). After optimization, the expected error is reduced to 7.2% (the residual being forced toward zero). The observed global, annual, ocean water budget (equation 15A) closes with a residual of 6.6% of P_O, with an expected error of 13.8%. Optimization reduces the expected error to 7.8%. The observed global, annual, atmospheric water budget (equation 18A) closes with a residual of 4.7% of P_W, with a 13.6% expected error being reduced to 7.5% by optimization. Hence the expected errors after optimization for the annual, global land, ocean, and atmospheric water budgets are less than 10%, which is consistent with a stated goal of NEWS (NSIT, 2007). That the observed residuals are considerably smaller than the expected errors suggests that we may have a better handle on global, annual water fluxes than previously supposed.

Figure 2 shows optimized, mean annual precipitation, evapotranspiration, runoff, and amplitude of the annual cycle of terrestrial water storage for each continent. The same numbers are presented in Table 3, along with the original observed estimates, uncertainties, and water budget residuals. Also included in Table 3 are ocean P and E. While most previous studies have ignored the Australasian and Indonesian Islands (including New Zealand and Tazmania), it is notable that they receive nearly as much rainfall as mainland Australia and produce almost double the runoff. They also receive more precipitation than Antarctica despite having one eighth the land area.

As seen in Table 3, with the notable exception of North America, for every continent as well as the world ocean, the expected closure error exceeds the magnitude of the surface water budget residual. In North America, difficulty measuring snowfall, which accounts for a large portion of precipitation, and runoff from Greenland and the islands of northern Canada are possible explanations for the larger than anticipated water budget residual. Still, the magnitude of the world land surface water budget residual, -3.4 mm/day, is well below that of the expected closure error, 8.0 mm/day. The atmospheric water budget residuals are within the error bounds for all ocean basins. These outcomes lend credence to the initial uncertainty estimates, which may in fact be overly conservative at the global land and global ocean scales. On the other hand, the atmospheric water budget residuals exceed the expected closure errors over mainland Australia, the Australasian and Indonesian Islands, and the Black Sea. Larger than expected residuals over the Islands and the Black Sea may be attributed to their small scale and limited observational constraints. The large residual over mainland Australia seems to arise from an imbalance in MERRA, which provides the sole atmospheric moisture convergence estimate due to the lack of a QuikSCAT Water Balance estimate for Australia. For the same period, MERRA P minus ET over Australia averages 11.9 mm/day, compared with a C estimate of 23.8 mm/day. The former number is more compatible with our original P and E estimates and would produce an atmospheric water budget residual of only -0.9 mm/day if substituted for MERRA convergenc

b. Mean Monthly Fluxes

The seasonal cycles of precipitation, evapotranspiration, runoff, atmospheric convergence, and water storage change over each continent and the global land and global ocean are plotted in Figure 3 (recall equations 3 and 4). Continents in the northern hemisphere have peak P, ET, and Q in the summer, and accumulate water in the winter. The same is true for the continents in the southern hemisphere, except that Q peaks later, in austral autumn, in South America, and the fluxes in Antarctica have a weak, bimodal annual cycle with P and ET minima in austral summer. Africa, which straddles the equator, has bimodal fluxes. Terrestrial water storage changes are dominated by the outputs, ET and Q, at the global scale and in most continents, but dS is controlled by P in South America, Africa, and the Australasian and Indonesian Islands.

It may seem counterintuitive that terrestrial precipitation peaks a month after terrestrial runoff at the global scale, considering that rainfall drives runoff. While the water fluxes associated with individual precipitation events or anomalously wet or dry periods are likely to behave that way (e.g., Changnon, 1987), the seasonal cycles of the fluxes are influenced by other factors. In North America, the snowpack immobilizes a large portion of annual continental precipitation and subsequently melts and releases it in the spring (snowpack is not isolated from terrestrial water storage in this analysis). As a result, Q peaks in June, while P, due to the strength of summer convective rainfall, peaks in July. The same is true in northern Eurasia. Further, the precipitation to runoff ratio happens to be smaller in June than July in all continents except for South America and Australia, hence the phenomenon of P lagging Q can also be attributed in part to a fluke of global averaging.

Similarly, the global, annual cycle of evapotranspiration does not lag but is more or less contemporaneous with precipitation, and precipitation actually lags evapotranspiration in South America. There, continental scale water fluxes are dominated by those in Amazonia, where water generally is abundant throughout the year. Thus ET is, for the most part, energy limited. That explains why ET peaks in January (when downward radiation is greatest in the southern hemisphere), two months before maximum P. However, downward radiation does not fluctuate much seasonally in the equatorial regions, so that the annual cycle of ET is weak (Rodell et al., 2011) despite an annual mean intensive rate of ET in South America that far exceeds that of the other continents (excepting the Australasian and Indonesian Islands). Further, because seasonal changes in ET and Q in South America are out of phase and both are small compared with seasonal changes in P, the annual cycles of P, C, and dS have nearly identical amplitude and phase. The seasonal phase of Q is closer to that of terrestrial water storage (S; not shown) than that of P, with a maximum in April-May and a minimum in September-October. Modulation of Q by S (via baseflow or, in the case of the Amazon, release of floodplain storage), which is a central tenet of the bucket model of terrestrial hydrology (Manabe, 1969), holds true for Africa and Australia as well.

In Eurasia, evapotranspiration follows the seasonal cycles of precipitation and solar radiation, peaking in July and bottoming in January. The relationship between P, S, and Q is more complicated. The seasonal cycle of S (not shown) achieves its maximum and minimum in April and October, respectively, while maximum and minimum Q occur in September and February. In this case, P seems to control Q more strongly, with a 1-2 month lag. That may be a consequence of an annual cycle of S with amplitude less than half that of North America and about a quarter that of South America. Despite the size of Eurasia, the average residence time of water after it falls on the land surface appears, perhaps deceptively, to be relatively short. More likely, the unusual timing of Q with respect to S may be the result of two very different climates being averaged together: northern Eurasia where the snowpack stores and releases runoff, and southern Eurasia where powerful monsoons regulate the seasonal cycles of P, S, and Q.

As mentioned previously, monthly runoff (ice flow to the ocean) from Antarctica and Greenland was computed as a water budget residual. Of the other fluxes, monthly mean dS over Antarctica from GRACE is believed to be robust; P is not well constrained by observations, but there is a reasonably small RMS difference of 13% between monthly P from GPCP and MERRA; and ET is likewise not well constrained but is believed to be inconsequential, averaging only 5% of P according to both MERRA and Princeton estimates.

Averaged over the world's oceans, precipitation appears to be nearly constant throughout the year (although a difference of just 1 mm/day equates to 361 km^3/day when spread over the global ocean). E is greatest in December and January, when downward radiation is strongest over the southern oceans and the air over the northern oceans is dry, and it remains relatively low from April through October. Terrestrial runoff into the oceans peaks in June and July, and because of that and the low austral winter E and nearly constant P, ocean storage begins to increase in May and reaches a maximum in October (coinciding with minimum northern snow water storage). Ocean C and dS are in phase with Q, peaking in June (May for C) and bottoming in December and January.

As seen in Figure 4, among the major ocean basins, the largest flux rates occur in the North Pacific and the smallest occur in the Arctic. The ranges of monthly flux rates in the other four basins are similar, though those in the South Atlantic are typically on the low side. In the North Pacific and Arctic, minimum P occurs in April and February, respectively, and maximum

P occurs in August for both. The seasonal cycle of P in the north Atlantic lags that of the other two northern ocean basins by three months. Precipitation in the southern oceans has the opposite phase, with greater than average P in austral autumn and lower than average P in austral spring.

Evaporation in the Arctic peaks in May, just prior to the month of maximum insolation, with a secondary peak in October, when sea ice is near its minimum. In all of the other ocean basins, E is largest in winter and smallest in summer. The negative correlation with the seasonal cycle of solar radiation and heating of the surface may seem counterintuitive until one recognizes two facts. First, most ocean evaporation occurs in the tropics, where solar radiation is nearly constant through the year. Second, evaporation is enhanced by dry, cold air outbreaks (particularly over the Gulf stream in the western North Atlantic and the Kuroshio current in the western North Pacific) and mid-latitude storms (due to their winds).

In general, the seasonal cycles of atmospheric convergence over the major ocean basins form smoother sinusoids than those of precipitation or evaporation, with familiar summer maxima and winter minima. A notable exception is the bimodal convergence in the North Atlantic, where separate maxima occur in June and September. P exceeds E (i.e., C is positive) in every month of the year in the Arctic Ocean. The North Pacific is the only other major ocean basin that has positive annual mean C (also see Table 3). That is somewhat surprising, considering that more than half of the North Pacific lies in the tropics, where the rate of evaporation is normally very high over open water. In fact, E over the North Pacific is comparable to that over the other ocean basins excluding the Arctic, but P is significantly larger, which tips the balance towards a positive annual mean C. This probably reflects the fact that the intertropical convergence zone is aligned at roughly 7.5°N over the Pacific.

6. Discussion

a. Water Budget Closure

This study demonstrates that global and continental/ocean basin, annual and monthly mean water balance closure can be achieved with acceptably small residuals and uncertainty (3.9% and 7.4% of precipitation, respectively, for the global surface water budget and significantly less than 10% in most other cases) based on modern satellite and model derived datasets. Uncertainty estimates provided with those datasets appear to be sufficiently conservative, as the actual water budget residuals are smaller than the predicted errors in all but a few cases. Our optimization approach imposes terrestrial, atmospheric, and oceanic water and energy budget closure at continental, oceanic, and global scales, on a mean monthly and mean annual basis. The uncertainty in all elements of the resulting dataset is smaller than the original observation error estimates (an inherent outcome of the approach), and in most cases both the original and optimized error estimates are reasonable when compared with residuals of the original observation based balance equations. Thus current quantitative understanding of the global water budget seems to be as good as or, in many cases, better than had previously been supposed. On the other hand, a pessimist might argue that 6% uncertainty in global ocean precipitation equates to more than half of the world's river discharge, so we still have work to do before we can claim we have a handle on the global water cycle. In the following paragraphs, imbalances and closure errors are presented as percentages of precipitation.

Assessing the surface water balance first, at the global, annual scale, the water budget closure error was predicted to be about 12.5% of precipitation. The actual residual of observational estimates is 3.9%, and the estimated uncertainty in the optimized global, annual surface water budget is 6.1%. Over the global land surface, the predicted annual water budget closure error was 10.1%, while the observed residual is 4.3%. After optimization, the estimated uncertainty declines to 7.2%. For the global ocean, the predicted closure error was 13.8%, while the observed residual and optimized uncertainty are 6.6% and 7.8%. Optimization increases the global ocean estimate of precipitation from GPCP by 4.7%, which is nearly identical to the conclusion of Behrangi et al. (2012; 2014).

The global, annual scale, atmospheric water budget was predicted to have 13.6% closure error, but the actual observed residual is much smaller, 4.7%, and the optimized error is 7.5%. The world land-atmosphere water imbalance was predicted to be 8.6%, while the observed residual is only 0.3% and the optimized error estimate is 7.2%. The world ocean-atmosphere water imbalance was predicted to be 14.6%, while the observed residual is 5.9% and the optimized closure uncertainty is 7.8%. As previously noted, the observed residuals and optimized error estimates in each of these global, annual cases are better than the NEWS goal of 10% water balance uncertainty (NSIT, 2007).

Predicted uncertainty in the monthly mean water budgets over the global land surface ranged from 11.1% in March to 15.1% in June, with an average of 12.9%. Observed residuals range from 0.3% in March and December to 18.4% in June, averaging 4.7%. Larger errors and residuals in May-August seem to arise from uncertainty in ET and Q. ET estimates from the three sources, Princeton, MERRA, and GLDAS, differ more during those months, and both ET and Q are elevated during boreal summer, so there is more room for error in absolute terms. Indeed, optimization reduces the June Q estimate by 18% and the June ET estimate by 6%. During a typical month, optimization changes those fluxes by less than 5% and 2%, respectively. Optimized terrestrial water budget uncertainty is close to 9% in every month. Predicted uncertainty in the monthly mean, global land-atmosphere water balance ranged from 9.7%

(September) to 12.4% (December), averaging 11.2%. Observed residuals range from 0.9% in October to 8.0% in January, with a mean of 3.6%. Optimized uncertainty is close to 8% in all months. Thus, over the global land, with the exception of the surface water budget during the boreal summer months when global Q and ET rise, the observed terrestrial and atmospheric-terrestrial water budgets close with less than 10% error, often much less, and the optimized water budget uncertainty is around 8-9% in all cases.

Among the continents, annual, surface water balance closure error was expected to be largest over Antarctica (32.4%), Australia and the Islands (16.1%), and Eurasia (12.5%). Optimized uncertainty in Antarctica declines to 17.3%, but the Antarctic water budget is a weak point of this study due to the lack of observed Q and a significant dependence on MERRA. On the other hand, the fluxes are relatively tiny in Antarctica, so that the errors are small in absolute terms. The observed residual and optimized uncertainty for Australia and the Islands are 8.6% and 9.6%. Those for Eurasia are 5.1% and 8.7%. Hence, aside from Antarctica and the Australasian and Indonesian Islands when separated from Australia, all observed residuals and optimized errors for the annual, continental surface water budgets are below the 10% target. The smallest predicted and optimized errors are those of South America (8.0% and 5.7%), and the smallest observed surface water budget residual is that of Africa (2.1%), though it should not be inferred that Africa's water cycle is therefore well observed and constrained. Despite higher densities of meteorological observations in North America and Eurasia, it is possible that water budget closure is hindered by more complex hydrology, i.e., seasonal snow and ice.

The annual land-atmosphere closure error was predicted to be largest over Antarctica (30.9%) and Australia and the Islands (14.6%). The observed residual and optimized uncertainty for Antarctica are 16.3% and 17.2% of precipitation, and they are 18.9% and 9.6% over Australia and the Islands. Surprisingly, the residual is larger over mainland Australia (24.9%) than over the Islands (17.3%). As described in section 5.1, this seems to arise from an overestimate of C from MERRA. The smallest predicted, observed (residual), and optimized errors are found over the same two continents as above, Africa (8.5%) and South America (1.3% and 5.7%).

The individual ocean basin surface water budgets are not closed due to the lack of ocean transport observations. The annual ocean-atmosphere water imbalance was predicted to be largest over the Arctic Ocean (52.6%) and the Mediterranean Sea (37.7%). The observed residuals are smaller (33.4% and 9.8%), as are the optimized uncertainty estimates (15.8% and 13.7%). The Black Sea has the largest observed residual as a percentage, 51.5%, but in absolute terms it is not very large. Expected errors for the major ocean basins other than the Arctic were all in the range of 11-19%, and optimization reduces that range to 7-15%. Observed residuals in those ocean basins range from 3.2% (North Atlantic) to 18.2% (South Atlantic).

The global ocean-atmosphere water balance was predicted to close with about 14% uncertainty during each month of the year. Observed residuals vary between 2.9% in July and 9.5% in March. Optimized water budget uncertainty is close to 10% in all months. Thus the observed residuals and optimized errors for the annual and monthly, global ocean and individual ocean basin-atmosphere water budgets satisfy the 10% target level in the majority of cases, the most notable exceptions being the large residual and optimized errors in the South Atlantic.

b. Evaluation of Metrics

Comparison of the optimized fluxes with those of Trenberth et al. (2011; henceforth T11) and Oki and Kanae (2006; henceforth OK06) reveals their global fluxes (Figure 1) all lie within our uncertainty ranges, save for the OK06 land precipitation value, which is slightly below the low end of our range. It is notable that the budget closure process causes our ocean P and E to go from observed values that are smaller (385,300 and 409,500 km^3/yr) than both T11 (386,000 and 426,000 km^3/yr) and OK06 (391,000 and 436,500 km^3/yr) to optimized values that are quite a bit larger (403,600 and 449,500 km^3/yr). Some of the discrepancies between the three studies may be attributed to the use of different time periods (2002-08 in T11; data from multiple periods, mostly before 2000, are used in OK06) and ocean/land masks.

The optimization process increases our ocean precipitation number by about 4.7% over the observed number (GPCP), which is well within the GPCP error bars of 8-10% for global ocean precipitation (Adler et al., 2012). The GPCP ocean magnitudes also compare well (within a few percent) with TRMM climatology estimates in the tropics (Adler et al. 2009; Wang et al., 2014). In addition, recent studies using TRMM plus Cloudsat information by Behrangi et al. (2012; 2014) report ocean precipitation that is 5% above GPCP. Our upward adjustment of GPCP ocean precipitation and surface latent heat flux is largely influenced by the energy budget, in that turbulent heat fluxes that were significantly larger than the initial estimates were required to balance net radiation (see L'Ecuyer et al., 2014, for further discussion). Stephens et al. (2013) increased GPCP global (land plus ocean) precipitation by 15% to balance surface radiation in their study, which is far more than the 4.7% ocean adjustment and <1% land adjustment applied in this study.

Our second metric was a comparison of the initial and optimized uncertainty estimates with the residuals of the observed water budget equations. We determined that, in most cases, the predicted errors were smaller than the residuals (see Sections 5 and 6.1). Further, the differences between the observed and optimized estimates of most fluxes were generally smaller than the associated uncertainties, even in the cases of ocean P and E. Overall, our approach –

beginning with a foundation of observations and adjusting their magnitudes based on relative errors to achieve water budget closure, and through the merger with the energy budget – seems to provide reasonable, balanced estimates of the components of both the global and regional water cycles.

c. Shortcomings

In addition to the coarse spatial and temporal resolutions of this analysis, the way that certain variables are lumped together (e.g., rainfall and snowfall), and a focus on changes in terrestrial and ocean water storage with no attempt to estimate the size of each reservoir (e.g., Shiklomanov and Rodda, 2003), there remain sources of possible error and other shortcomings relative to the ideal global water budget analysis. Some result from decisions made in framing the study. In particular, a major objective has been to rely on modern, observation-integrating datasets, particularly those derived from satellite observations, which necessarily limits the use of in situ observations and prevents estimation of the sizes of various stocks of water. Similarly, we gave preference to datasets developed by members of the NEWS team in order to ensure that expertise would be available to inform the optimization and to interpret the results and that the specifically defined continental and ocean basin, decadal-means would be provided, along with uncertainty estimates. As a consequence, other datasets which may in fact have had smaller errors were intentionally omitted from the analysis. For example, some evidence suggests that model-based precipitation estimates may be better than observations at higher latitudes, but we chose to rely exclusively on GPCP. Further, there are tens of global evapotranspiration datasets available (e.g., Jimenez et al., 2011; Mueller et al., 2011) whose inclusion probably would reduce uncertainty in our continental scale estimates, but we determined to use three that have a high proportion of satellite based inputs: one directly derived from observations and two based on observation integrating models (one coupled, one land surface only).

We chose to examine the first decade of the new millennium rather than developing a true climatology, which is commonly taken to require at least 30 years of data. That decision was made in part because the 2000s are the EOS era (thus it is a corollary of the first decision/objective) and in part because it presumes future, routine, decadal state of the water cycle studies, with the goal of detecting water cycle shifts related to climate change. Still, it would not be appropriate to use the results presented herein exactly as one would use a climatology, nor would it be scientifically justifiable to conclude that an observed shift or trend based on two or three such studies is real and likely to continue, unless accompanied by a well vetted explanation of the mechanism and other corroborating information. For example, Australia experienced its worst drought in over 100 years during 2001-09 (van Dijk et al., 2013). As a result the continental Australian water budget depicted here is likely to be weaker than that of the decade that follows, yet a wetting trend should not in the future be inferred.

On the other hand, there are some real trends in terrestrial water storage as measured by GRACE that we intentionally ignore. In particular, Greenland, Antarctica, and the glaciers along the Gulf of Alaska have been shedding ice at a total rate of 380 km^3/yr (Luthcke et al., 2013). Our estimates of dS are based on detrended time series, and our Q estimates are based on continental water budgets with mean annual dS equal to zero.

While optimization of the water fluxes through the simultaneous constraint of budget equations across multiple spatial and temporal scales is an important advance that certainly improved the outcomes of this study, our approach relies on assumptions that are unlikely to be true in all cases. In particular, unbiased, Gaussian statistics are assumed. Evidence to support that assumption is limited to a study by Sardeshmukh et al. (2000), who showed that rainfall is largely normally distributed at the 2.5° monthly scale for regions of mean upward motion (i.e., substantial amounts of rain). However, structural errors are likely to exist due to imperfect retrieval algorithms and uneven sampling of the diurnal cycle. Biases in our estimates and non-Gaussian or correlated errors would reduce the efficacy of the optimization routine and lead to less accurate flux estimates and associated uncertainty ranges. Nevertheless, lacking better information on the statistical distributions of the input datasets, little can be done to quantify or control these potential deficiencies.

d. The Value of Modern Datasets

EOS era observations and output from data assimilating models form the basis of this analysis. Without them an accounting of the global water budget at the turn of the century would rely heavily on incomplete surface data and guesswork. While such an accounting may be useful when global climate is stationary, it cannot be used to quantify water cycle fluxes now and how they change in the future. In situ and remote sensing data complement each other. Ground based meteorological or hydrological observations have been used to anchor, calibrate, or inform all of the datasets used herein in some way or other. Observations from satellites, including those in GOES series, TRMM, Terra, and Aqua, are crucial for filling often extensive spatial and temporal gaps in the surface observational record and for extending that record to the near-present. Moreover, global data on terrestrial and oceanic water storage change, long the missing link in water budget closure studies, is a product of GRACE that cannot feasibly be replicated by ground based observations.

Data integrating models serve a similar gap-filling role in this analysis, and also enable more and different types of data to be incorporated as constraints. MERRA provides flux data for regions of the world that are poorly monitored, including Antarctica and the Australasian and Indonesian Islands. MERRA and GLDAS evapotranspiration estimates are a valuable and independent addition to observation-based ET, and together they enable uncertainty to be assessed with a higher degree of confidence. ECMWF Interim, the new Japanese reanalysis of 55 years extent (JRA55), and MERRA2 offer new input sources that could be used in a similar study in the future. The ongoing development of such data integrating models and reanalyses undoubtedly will benefit future water and energy budget assessments and will be vital for maximizing the value of Earth observing systems, a fact that must be considered in budgeting future missions and planning the Global Earth Observation System of Systems (GEOSS).

While the GOES satellites have been serving continuously since 1975 and will extend their record with the anticipated launch of GOES-R in late 2015, it is notable that TRMM, Terra, Aqua, and GRACE all launched between 1997 and 2002 and are well beyond their design lifetimes. Considering the importance of observational continuity to any study of recent climate variability and change, it is good that reinforcements are beginning to arrive. Terra's and Aqua's observational capabilities have been augmented (and eventually may be replaced) by NASA's Suomi National Polar-orbiting Partnership mission (Suomi-NPP, launched in 2011), which carries CERES and the Visible Infrared Imager Radiometer Suite (VIIRS; a technology similar to MODIS), and by JAXA's Global Change Observation Mission 1 – Water (GCOM-W1), which carries the AMSR2 system. TRMM is being succeeded by the NASA/JAXA Global Precipitation Measurement mission (GPM), which launched on 28 February 2014. A successor to the GRACE mission, GRACE Follow On, is planned to launch in 2017. Other current and future Earth observing satellites that could help to constrain global and regional water budgets include the European Space Agency's Soil Moisture Ocean Salinity mission (SMOS; launched 2009), NASA's Soil Moisture Active Passive mission (SMAP; scheduled to launch in 2014), and NASA's Surface Water Ocean Topography mission (SWOT; proposed to launch in 2020). SWOT would be particularly valuable for water budget studies, as it promises to improve estimates of river discharge in parts of the world where such data are not made available for political reasons and otherwise. Together, these next generation Earth observing satellites offer intriguing prospects for building on and improving the analysis presented here. Still, there is strong justification for increasing the pace of mission approval and deployment (NRC, 2007). Further, the prospect of performing a similar study at finer than monthly, continental/ocean basin scale, without greatly increasing reliance on numerical models, would be improved by higher spatial and temporal resolution of observations, meaning more satellites and enhanced technologies. The path to that goal is fairly direct, but requires technical innovation and sustained funding.

e. Future Directions

As noted above, increasing the spatial and temporal resolutions of this analysis are obvious objectives for the future. A second goal should be to extend the analysis forward in time and begin to describe changes in the water budget from one period to the next. For some time, it will be difficult to determine with certainty which changes are part of a real, long term trend and which are related to inter-decadal natural variability, but that should not discourage the effort. The analysis of Robertson et al. (2014) is a step in that direction. Third, as old satellites are decommissioned and new ones are launched, it will be important to identify ensuing discontinuities in the data record. Many other follow-on studies are merited, including partitioning of the water storages and fluxes, assessing diurnal cycles, investigating extremes, computing advanced statistics, and estimating the size of each storage reservoir and associated residence times. Because of the importance with which water and energy fluxes in Earth's climate system cross-cut other disciplines, in ways both physical and biogeochemical, there are likely numerous directions in which the present study could be refined.

The current results should be applied toward the assessment of global climate prediction models such as those contributing to the Coupled Model Intercomparison Project Phase 5 (CMIP5; Taylor et al., 2012), whose first goal is to "evaluate how realistic the models are in simulating the recent past". Our water and energy budget analysis, whose resulting dataset is available online (http://disc.gsfc.nasa.gov/hydrology) [to be uploaded after publication], was performed with that goal in mind, and such comparisons are an essential step towards the NEWS objective of improving predictions of future climate change.

Acknowledgements

This research was funded by multiple grants from NASA's Energy and Water Cycle Study (NEWS) program.

Appendix

$\mathbf{F_{obs}}$ is a vector consisting of eight parameters over eight regions (seven continents and global ocean), one parameter over only continents, and two additional parameters at the global scale, all derived from observations. The key for the regions are listed in Table 1. The parameters are the component fluxes of the water and energy balance equations: convergence

(C), evapotranspiration (E), precipitation (P), runoff (Q), surface longwave downward radiation (DLR), surface shortwave downward radiation (DSR), surface longwave upward radiation (ULW), surface shortwave upward radiation (USW), surface sensible heat (SH), top of atmosphere (TOA) net shortwave radiation (TSR), and TOA outgoing longwave radiation (OLR). Subscripts refer to the seven continents (e.g., *na* for North America), global ocean, and world, where world is a sum of all regions. Since we don't have an observation for Q*ocean*, it is set equal to Q*land*, which is the sum of Q over all continents. The one dimensional vector $\mathbf{F_{obs}}$ is expressed in groups below for demonstration purpose (but it is a column vector and not a 2-dimensional matrix).

$$\mathrm{F}_{obs} = \left\{ \begin{matrix} C_{na}, E_{na}, P_{na}, Q_{na}, DSL_{na}, DSR_{na}, ULW_{na}, USW_{na}, SH_{na}, \\ C_{sa}, E_{sa}, P_{sa}, Q_{sa}, DSL_{sa}, DSR_{sa}, ULW_{sa}, USW_{sa}, SH_{sa}, \\ \cdots \\ \ldots \\ \ldots \\ C_{ocean}, E_{ocean}, P_{ocean}, DSL_{ocean}, DSR_{ocean}, ULW_{ocean}, USW_{ocean}, SH_{ocean}, \\ TSR_{world}, OLR_{world} \end{matrix} \right\}^{T} \tag{S1}$$

R is a column vector consisting of residuals of the three balance equations over the seven continents and global ocean and residuals of the two balance equations that serve as global constraints. The balance equations are defined in Section 4.2.

$$\mathrm{R} = \left\{ \begin{matrix} dW_{na},\ dS_{na}, NET_{na}, \\ dW_{sa,} dS_{sa,} NET_{sa}, \\ \ldots. \\ dW_{ocean}, dS_{ocean}, NET_{ocean}, \\ C_{land} + C_{ocean}, \\ NETA_{world} \end{matrix} \right\}^{T} \tag{S2}$$

References

Adler, R.F., G.Gu, and G.J. Huffman, 2012: Estimating climatological bias errors for the Global Precipitation Climatology Project (GPCP). *J. Appl. Meteor. Climatol.*, **51**, 84–99, doi:10.1175/JAMC-D-11-052.1.

Adler, R.F., G.J. Huffman, A. Chang, R. Ferraro, P. Xie, J. Janowiak, B. Rudolf, U. Schneider, S. Curtis, D. Bolvin, A. Gruber, J. Susskind, P. Arkin, and E. Nelkin, 2003: The version-2 Global Precipitation Climatology Project (GPCP) monthly precipitation analysis (1979-Present). *J. Hydrometeor.*, **4**, 1147-1167, doi: http://dx.doi.org/10.1175/1525-7541(2003)004<1147:TVGPCP>2.0.CO;2

Adler, R. F., J.-J. Wang, G. Gu, and G.J. Huffman, 2009: A ten-year tropical rainfall climatology based on a composite of TRMM products. *J. Meteorol. Soc. Japan*, **87A**, 281-293.

Alsdorf, D. E., E. Rodríguez, and D. P. Lettenmaier, 2007: Measuring surface water from space. *Rev. Geophys.,* **45**, RG2002, doi:10.1029/2006RG000197.

Baumgartner, A., and E. Reichel, 1975: *The World Water Balance.* Elsevier, 179 pp.

Bedka, S., R. Knuteson, H. Revercomb, D. Tobin, and D. Turner, 2010: An assessment of the absolute accuracy of the Atmospheric Infrared Sounder v5 precipitable water vapor product at tropical, midlatitude, and arctic ground-truth sites: September 2002 through August 2008. *J. Geophys. Res.,* **115,** D17310, doi:10.1029/2009JD013139.

Behrangi, A., M. Lebsock, S. Wong, and B. Lambrigtsen, 2012: On the quantification of oceanic rainfall using spaceborne sensors. *J. Geophys. Res.*, **117,** D20105.

Behrangi, A., G. Stephens, R. Adler, G. Huffman, B. Lambrigtsen, and M. Lebsock, 2014: An update on oceanic precipitation rate and its zonal distribution in light of advanced observations from space. *J. Climate,* **27**, 3957-3965.

Berner, E.K., and R.A. Berner, 1987: *The Global Water Cycle: Geochemistry and Environment*. Prentice-Hall, Inc., 397 pp.

Bertsekas, D. P., 1996: *Constrained Optimization and Lagrange Multiplier Methods*. Athena Scientific, 395 pp.

Bettadpur, S., 2012: *UTCSR Level-2 Processing Standards Document for Level-2 Product Release 0005.* GRACE 327-742 (CSR Publ. GR-12-xx), 16pp, [ftp://podaac.jpl.nasa.gov/allData/grace/docs/L2-CSR0005_ProcStd_v4.0.pdf].

Bonan, G.B., 1998: The land surface climatology of the NCAR Land Surface Model coupled to the NCAR Community Climate Model. *J. Climate,* **11**, 1307-1326.

Bosilovich, M.G., and S.D. Schubert, 2001: Precipitation recycling over the central United States as diagnosed from the GEOS1 Data Assimilation System. *J. Hydrometeor.*,

2, 26-35.

Bosilovich, M., S.D. Schubert, and G.K. Walker, 2005: Global changes of the water cycle intensity. *J. Climate*, **18**, 1591–1608.

Bosilovich, M.G., F.R. Robertson, and J. Chen, J., 2011: Global energy and water budgets in MERRA. *J .Climate*, **24**, 5721-5739, doi:10.1175/2011JCLI4175.1.

Bruckner, E.A., 1905: Die Bilanz des Kreislaufs des Wassers auf der Erde. *Geographische Zeitschrift*, **11**, 436-445.

Chahine, M. T., 1992: The hydrological cycle and its influence on climate. *Nature,* **359**, 373–380.

Chambers, D. P., 2009: Calculating trends from GRACE in the presence of large changes in continental ice storage and ocean mass. *Geophys. J. Int*., **176**, 415-419, doi: 10.1111/j.1365-246X.2008.04012.x.

Chambers, D.P., and J.A. Bonin, 2012: Evaluation of release-05 GRACE time-variable gravity coefficients over the ocean. *Ocean Science*, **8,** 1–10, doi:10.5194/os-8-1-2012.

Chambers, D. P., and J. Schröter, 2011: Measuring ocean mass variability from satellite gravimetry, *J. Geodynamics*, **52,** 333-343, doi:10.1016/j.jog.2011.04.004.

Changnon, S.A., 1987: *Detecting drought conditions in Illinois*. Illinois State Water Survey circular No. 169, 36 pp.

Chen, F., K. Mitchell, J. Schaake, Y. Xue, H. Pan, V. Koren, Y. Duan, M. Ek, and A. Betts, 1996: Modeling of land-surface evaporation by four schemes and comparison with FIFE observations. *J. Geophys. Res.*,**101**, 7251-7268.

Chen, M., W. Shi, P. Xie, V.B.S. Silva, V.E. Kousky, R.W. Higgins, and J.E. Janowiak, 2008: Assessing objective techniques for gauge-based analyses of global daily precipitation. *J. Geophys. Res.*, **113**, D04110, doi:10.1029/2007JD009132.

Clark, E.A., J. Sheffield, M. van Vliet, B. Nijssen, and D.P. Lettenmaier, 2014: Continental runoff into the oceans (1950-2008). *J. Hydrometeor.*, in preparation.

Clayson, C. A., J. B. Roberts, and A. Bogdanoff, 2014: SeaFlux Version 1: A new satellite-based ocean-atmosphere turbulent flux dataset. *Int. J. Climatol.*, in revision.

Dai, A., T. Qian, K.E. Trenberth, and J.D Milliman, 2009: Changes in continental freshwater discharge from 1948-2004. *J. Climate*, **22**, 2773-2791.

Dickinson, R.E., 1984: Modeling evapotranspiration for three-dimensional global climate models. *Climate Processes and Climate Sensitivity*, J. E. Hansen and T. Takahashi, eds., Geophys. Monogr. Ser., Vol. 29, American Geophysical Union, 58-72.

Dirmeyer, P.A., X. Gao, M. Zhao, Z. Guo, T. Oki, and N. Hanasaki, 2006: GSWP-2: multimodel analysis and implications for our perception of the land surface. *Bull. Amer. Meteor. Soc.,* **87**, 1381–1397.

Divakarla, M., C. Barnet, M.D. Goldberg, L. McMillin, E.S. Maddy, W.W. Wolf, L. Zhou, and X. Liu, 2006: Validation of Atmospheric Infrared Sounder temperature and water vapor retrievals with matched radiosonde measurements and forecasts. *J. Geophys. Res.,* **111**, D09S15, doi:10.1029/2005JD006116.

Eagleson, P.S., 1986: The emergence of global-scale hydrology. *Water Resour. Res.*, **22**, 6–14.

Ek, M.B., K.E. Mitchell, Y. Lin, E. Rogers, P. Grunmann, V. Koren, G. Gayno, and J.D. Tarpley, 2003: Implementation of Noah land surface model advances in the National Centers for Environmental Prediction operational mesoscale Eta model. *J. Geophys. Res.*, **108**, 8851, doi:10.1029/2002JD003296.

Fairall, C.W.; E.F. Bradley, J.E. Hare, A.A. Grachev, and J.B. Edson, 2003: Bulk parameterization of air-sea fluxes: updates and verification for the COARE algorithm. *J. Climate*, **16**, 571-591.

Famiglietti, J.S., and M. Rodell, 2013: Water in the balance. *Science*, **340,** 1300-1301, doi:10.1126/science.1236460.

Fekete, B.M., C.J. Vöröosmarty, and W. Grabs, 2002: High-resolution fields of global runoff combining observed river discharge and simulated water balances. *Global Biogeochem. Cycles,* **16**, 15-1, doi:10.1029/1999GB001254.

Fetzer, E.J., B. Lambrigtsen, A. Eldering, H.H. Aumann, and M.T. Chahine, 2006: Biases in total precipitable water vapor climatologies from Atmospheric Infrared Sounder and Advanced Microwave Scanning Radiometer, *J. Geophys. Res.,* **111,** D09S16, doi:10.1029/2005JD006598.

Fuller K., H. Shear, and J. Wittig, 1995: *The Great Lakes - An Environmental Atlas and Resource Book,* EPA 905-B-95-001, 46 pp.

GEWEX, 2012a: GEWEX Plans for 2013 and beyond: Imperatives. GEWEX Document Series No. 2012-1.

GEWEX, 2012b: GEWEX Plans for 2013 and beyond: Science Questions. GEWEX Document Series No. 2012-2.

Gordon, N.D., A.K. Jonko, P.M. Forster, and K.M. Shell, 2013: An observationally based constraint on the water-vapor feedback. *J. Geophys. Res.,* **118***,* 12,435-12,443, doi:10.1002/2013JD020184.

Hansen, M.C., R.S. DeFries, J.R.G. Townshend, and R. Sohlberg, 2000: Global land cover classification at 1km spatial resolution using a classification tree approach. *International Journal of Remote Sensing*, **21**, 1331-1364.

Hearty, T.J., A. Savtchenko, B. Tian, E. Fetzer, Y.L. Yung, M. Theobald, B. Vollmer, E. Fishbein, and Y.-I. Won, 2014: Estimating sampling biases and measurement uncertainties of AIRS/AMSU-A temperature and water vapor observations using MERRA reanalysis. *J. Geophys. Res.,* **119**, 2725-2741, doi:10.1002/2013JD021205.

Held, I., and B. Soden, 2006: Robust responses of the hydrological cycle to global warming. *J. Climate*, **19**, 5686- 5699.

Hilburn, K.A., 2009: The passive microwave water cycle product. Remote Sensing Systems report number 072409, 30 pp, [available from http://www.remss.com].

Hoekstra, A.Y., and M.M. Mekonnen, 2012: The water footprint of humanity. *Proceedings of the National Academy of Sciences,* doi:10.1073/pnas.1109936109.

Huffman, G.J., R.F. Adler, P. Arkin, A. Chang, R. Ferraro, A. Gruber, J. Janowiak, A. McNab, B. Rudolf, and U. Schneider,1997: The Global Precipitation Climatology Project (GPCP) combined precipitation dataset. *Bull. Amer. Meteor. Soc.*, **78**, 5–20, doi:http://dx.doi.org/10.1175/1520-0477(1997)078<0005:TGPCPG>2.0.CO;2.

Huffman, G.J., R.F. Adler, D.T. Bolvin, and G. Gu, 2009: Improving the global precipitation record: GPCP version 2.1. *Geophys. Res. Lett.*, **36**, L17808, doi:10.1029/2009GL040000.

Huntington, T.G., 2005: Evidence for intensification of the global water cycle: review and synthesis. *J. Hydrology*, **319**, 83-95, doi:10.11029/2003L091188.

Idso, S., 1981: A set of equations for full spectrum and 8 to 14 µm and 10.5 to 12.5 µm thermal radiation from cloudless skies. *Water Resources Research*, **17**, 295-304.

Jimenez, C., C. Prigent, B. Mueller, S. I. Seneviratne, M. F. McCabe, E.F. Wood, W. B. Rossow, G. Balsamo, A. K. Betts, P. A. Dirmeyer, J. B. Fisher, M. Jung, M. Kanamitsu, R. H. Reichle, M. Reichstein, M. Rodell, J. Sheffield, K. Tu, and K. Wang, 2011: Global inter-comparison of 12 land surface heat flux estimates. *J. Geophys. Res.*, **116**, D02102, doi:10.1029/2010JD014545.

Johnson, G.F., and D.P. Chambers, 2013: Ocean bottom pressure seasonal cycles and decadal trends from GRACE release-05: ocean circulation implications. *J. Geophys. Res.,* **118,** 4228-4240, doi:10.1002/jgrc.20307.

Jung, M., and Coauthors, 2010: Recent decline in the global land evapotranspiration trend due to limited moisture supply. *Nature*, **467**, 951-954, doi:10.1038/nature09396.

Koren, V., J. Schaake, K. Mitchell, Q.Y. Duan, F. Chen, and J.M. Baker, 1999: A parameterization of snowpack and frozen ground intended for NCEP weather and climate models. *J. Geophys. Res.*,**104**, 19569-19585.

Korzoun, V. I., ed., 1974: *World water balance and water resources of the earth.* Hydrometeoizdat, 638 pp, [In Russian].

Koster, R.D., and M.J. Suarez, 1996: Energy and water balance calculations in the Mosaic LSM. NASA Technical Memorandum 104606, no. 9, 76 pp.

Kumar, S.V., R.H. Reichle, C. D. Peters-Lidard, R. D. Koster, X. Zhan, W. T. Crow, J. B. Eylander, and P. R. Houser, 2008: A land surface data assimilation framework using the Land Information System: description and applications. *Advances in Water Resources*, **31**, 1419-1432, doi:10.1016/j.advwatres.2008.01.013.

Landerer, F.W., and S. C. Swenson, 2012: Accuracy of scaled GRACE terrestrial water storage estimates. *Water Resources Research*, **48**, W04531, doi:10.1029/2011WR011453.

L'Ecuyer, T.S., and G.L. Stephens, 2002: An estimation-based precipitation retrieval algorithm for attenuating radars. *J. Appl. Meteorol.*, **41**, 272–285.

Liang, X., D.P. Lettenmaier, E.F. Wood, and S.J. Burges, 1994: A simple hydrologically based model of land surface water and energy fluxes for GSMs. *J. Geophys. Res.*, **99**, 14,415-14,428.

Liu, W.T., X. Xie, W. Tang, and V. Zlotnicki, 2006: Spacebased observations of oceanic influence on the annual variation of South American water balance. *Geophys. Res. Lett.*, **33**, L08710, doi:10.1029/2006GL025683.

Luthcke, S.B., T.J. Sabaka, B.D. Loomis, A.A. Arendt, J.J. McCarthy, and J. Camp, 2013: Antarctica, Greenland and Gulf of Alaska land-ice evolution from an iterated GRACE global mascon solution. *J. Glaciology*, **59**, 613-631.

Lyman, J.M., S.A. Good, V.V. Gouretski, M. Ishii, G.C. Johnson, M.D. Palmer, D.M. Smith, and J.K. Willis, 2010: Robust warming of the global upper ocean. *Nature*, **465**, 334-337.

Manabe, S., 1969: Climate and the ocean circulation: 1. the atmospheric circulation and the hydrology of the earth's surface. *Mon. Weather Rev.*, **97**, 739–805.

Mandelbrot, B.B., 1983: *The Fractal Geometry of Nature*. Macmillan, 468 pp.

Mehta, V.M., A.J. DeCandis, and A.V. Mehta, 2005: Remote-sensing-based estimates of the fundamental global water cycle: Annual cycle. *J. Geophys. Res.*, **110**, D22103, doi:10.1029/2004JD005672.

Mintz, Y., and Y.V. Serafini, 1992: A global monthly climatology of soil moisture and water balance. *Climate Dyn.,* **8**, 13-27.

Mitchell, K., and Coauthors, 2004: The multi-institution North American Land Data Assimilation System (NLDAS): utilizing multiple GCIP products and partners in a continental distributed hydrological modeling system. *J. Geophys. Res.,* **109**, D07S90, doi: 10.1029/2003JD003823.

Monteith, J.L.,1965: Evaporation and environment. *Symp. Sot. Exp. Biol.*, **19**, 205-234.

Mueller, B., S.I. Seneviratne, C. Jimenez, T. Corti, M. Hirschi, G. Balsamo, A. Beljaars, A.K. Betts, P. Ciais, P. Dirmeyer, J.B. Fisher, Z. Guo, M. Jung, C.D. Kummerow, F. Maignan, M.F. McCabe, R. Reichle, M. Reichstein, M. Rodell, W.B. Rossow, J. Sheffield, A. J. Teuling, K. Wang, and E.F. Wood, 2011: Evaluation of global observations-based evapotranspiration datasets and IPCC AR4 simulations. *Geophys. Res. Lett.*, **38**, L06402, doi:10.1029/2010GL046230.

Nace, R.L., 1969: World water inventory and control. *Water, Earth, and Man.*, R.J. Chorley, ed., Methuen, 31-42.

NASA Energy and Water Cycle Study (NEWS) Science Integration Team (NSIT), 2007: A NASA Earth Science Implementation Plan for Energy and Water Cycle Research: Predicting Energy and Water Cycle Consequences of Earth System Variability and Change. NASA, 89 pp., [available online: http://news.cisc.gmu.edu/doc/NEWS_implementation.pdf].

National Research Council (US), Committee on Earth Science and Applications from Space, 2007: *Earth Science and Applications from Space: National Imperatives for the Next Decade and Beyond.* National Academies Press, 456 pp.

Oki, T., 1999: Global water cycle. *Global Energy and Water Cycles,* K. Browning and R. Gurney, eds., Cambridge University Press, 10-27.

Oki, T., and S. Kanae, 2006: Global hydrological cycles and world water resources. *Science*, **313**, 1068-1072, doi:10.1126/science.1128845.

Peixoto, J.P., and A.H. Oort, 1992: *Physics of Climate.* American Institute of Physics, 520 pp.

Rama Varma Raja, M.K., S.I. Gutman, J.G. Yoe, L.M. McMillin, and J. Zhao, 2008: The validation of AIRS retrievals of integrated precipitable water vapor using measurements from a network of ground-based GPS receivers over the contiguous United States. *J. Atmos. Oceanic Technol.,* **25,** 416–428.

Reichle, R.H., R.D. Koster, G.J.M. De Lannoy, B.A. Forman, Q. Liu, S.P.P. Mahanama, and A. Toure, 2011: Assessment and enhancement of MERRA land surface hydrology estimates. *J. Climate*, **24**, 6322-6338, doi:10.1175/JCLI-D-10-05033.1.

Reichle, R.H., 2012: The MERRA-Land Data Product (Version 1.2). GMAO Office Note No. 3, 43 pp., [available at http://gmao.gsfc.nasa.gov/pubs/office_notes].

Reynolds, C.A., T.J. Jackson, and W.J. Rawls, 2000: Estimating soil water-holding capacities by linking the Food and Agriculture Organization soil map of the world with global pedon databases and continuous pedotransfer functions. *Water Resources Research*, **36**, 3653-3662.

Rienecker, M.R. and 28 co-authors, 2011: MERRA - NASA's Modern-Era Retrospective Analysis for Research and Applications. *J. Climate*, **24**, 3624–3648, doi:http://dx.doi.org/10.1175/JCLI-D-11-00015.1.

Roads, J.O., M. Kanamitsu, and R. Stewart, 2002: CSE water and energy budgets in the NCEP-DOE Reanalysis II. *J. Hydrometeor.,* **3**, 227-248.

Roberts, J.B., C.A. Clayson, F.R. Robertson, and D.L. Jackson, 2010: Predicting near-surface characteristics from SSMI using neural networks with a first guess approach. *J. Geophys. Res.,* **115**, D19113, doi:10.1029/2009JD013099.

Robertson, F.R., M.G. Bosilovich, J.B. Roberts, R.H. Reichle, R. Adler, L. Ricciardulli, W. Berg, and G.J. Huffman, 2014: Consistency of estimated global water cycle variations over the satellite era*, J. Climate*, in review.

Rodell, M., and J.S. Famiglietti, 1999: Detectability of variations in continental water storage from satellite observations of the time dependent gravity field. *Wat. Resour. Res.,* **35**, 2705-2723, doi:10.1029/1999WR900141.

Rodell, M., J.S. Famiglietti, J. Chen, S. Seneviratne, P. Viterbo, S. Holl, and C.R. Wilson, 2004a: Basin scale estimates of evapotranspiration using GRACE and other observations. *Geophys. Res. Lett.*, **31**, L20504, doi:10.1029/2004GL020873.

Rodell, M., P.R. Houser, U. Jambor, J. Gottschalck, K. Mitchell, C.-J. Meng, K. Arsenault, B. Cosgrove, J. Radakovich, M. Bosilovich, J.K. Entin, J.P. Walker, D. Lohmann, and D. Toll, 2004b: The Global Land Data Assimilation System. *Bull. Amer. Meteor. Soc.*, **85**, 381–394.

Rodgers, C.D., 2000: *Inverse Methods for Atmospheric Sounding- Theory and Practice*. World Scientific, 240 pp.

Sardeshmukh, P.D., G.P.Compo, and C. Penland, 2000: Changes of probability associated with El Niño. *J. Climate*, **13**, 4268-4286.

Schlosser, C.A., and P. Houser, 2007: Assessing a satellite-era perspective of the global water cycle, *J. Climate,* **20**, 1316-1338.

Sellers, P.J., Y. Mintz, Y.C. Sud, and A. Dalcher, 1986: A Simple Biosphere Model (SIB) for use within general circulation models. *J. Atmos. Sci.*, **43**, 505–531.

Shapiro, R., 1987: A simple model for the calculation of the flux of direct and diffuse solar radiation through the atmosphere. AFGL-TR-87-0200, Air Force Geophysics Lab, 40 pp.

Sheffield, J., G. Goteti, and E.F. Wood, 2006: Development of a 50-yr high-resolution global dataset of meteorological forcings for land surface modeling. *J. Climate,* **19**, 3088-3111.

Shiklomanov, I. A., and J.C. Rodda, eds., 2003: *World water resources at the beginning of the twenty-first century*. Cambridge University Press, 435 pp.

Stephens, G.L., J.L. Li, M. Wild, C.A. Clayson, N. Loeb, S. Kato, T. L'Ecuyer, P.W. Stackhouse, M. Lebsock, and T. Andrews, 2012: An update on Earth's energy balance in light of the latest global observations. *Nature Geoscience*, **5,** 691-696.

Susskind, J., J.M. Blaisdell, L. Iredell, and F. Keita, 2010: Improved temperature sounding and quality control methodology using AIRS/AMSU data: the AIRS science team version 5 retrieval algorithm. *IEEE Trans. Geosci. Remote Sens.,* **49,** 883-907.

Swenson, S., and J. Wahr, 2002: Methods for inferring regional surface-mass anomalies from Gravity Recovery and Climate Experiment (GRACE) measurements of time-variable gravity. *J. Geophys. Res.*, **107**, 2193, doi:10.1029/2001JB000576.

Syed, T.H., J.S. Famiglietti, D.P. Chambers, J.K. Willis, and K. Hilburn, 2010: Satellite-based global-ocean mass balance estimates of interannual variability and emerging trends in continental freshwater discharge. *Proceedings of the National Academy of Sciences,* **107**, 17916-17921, doi: 10.1073/pnas.1003292107.

Szczodrak, M., P.J. Minnett, and C. Gentemann, 2006: Comparison of AMSR-E retrievals of total water vapor over the ocean with ship based measurements. 10th Symposium on Integrated Observing and Assimilation Systems for the Atmosphere, Oceans, and Land Surface (IOAS-AOLS), Am. Meteorol. Soc., 4 pp. [Available at http://ams.confex.com/ams/Annual2006/techprogram/paper_105174.htm].

Tapley, B.D., S. Bettadpur, M. Watkins, and C. Reigber, 2004: The Gravity Recovery and Climate Experiment: Mission overview and early results. *Geophys. Res. Lett*., **31,** L09607, doi:10.1029/2004GL019920.

Tian, B., C.O. Ao, D.E. Waliser, E.J. Fetzer, A.J. Mannucci, and J. Teixeira, 2012: Intraseasonal temperature variability in the upper troposphere and lower stratosphere from the GPS radio occultation measurements. *J. Geophys. Res.,* **117**, D15110, doi:10.1029/2012JD017715.

Tian, B., E.J. Fetzer, B.H. Kahn, J. Teixeira, E. Manning, and T. Hearty, 2013: Evaluating CMIP5 Models using AIRS tropospheric air temperature and specific humidity climatology. *J. Geophys. Res.,* **118***,* 114–134, doi:10.1029/2012JD018607.

Tobin, D.C., H.E. Revercomb, R.O. Knuteson, B. Lesht, L.L. Strow, S.E., Hannon, W.F. Feltz, L. Moy, E.J. Fetzer, and T. Cress, 2006: Atmospheric Radiation Measurement site atmospheric state best estimates for Atmospheric Infrared Sounder temperature and water vapor retrieval validation. *J. Geophys. Res.*, **111**, D09S14, doi:10.1029/2005JD006103.

Trenberth, K.E., L. Smith, T. Qian, A. Dai, and J. Fasullo, 2007: Estimates of the global water budget and its annual cycle using observational and model data. *J. Hydrometeor.*, **8**, 758–769.

Trenberth, K.E., J.T. Fasullo, and J. Mackaro, 2011: Atmospheric moisture transports from ocean to land and global energy flows in reanalyses. *J. Climate.*, **24**, 4907-4924, doi:10.1175/2011JCLI4171.1.

Uemura, T., M. Taniguchi, and K. Shibuya (2011), Submarine groundwater discharge in Lützow-Holm Bay, Antarctica. *Geophys. Res. Lett.*, **38**, L08402, doi:10.1029/2010GL046394.

Van Dijk, A.I., H.E. Beck, R.S. Crosbie, R.A. de Jeu, Y.Y. Liu, G.M. Podger, B. Timbal, and N.R. Viney, 2013: The millennium drought in southeast Australia (2001–2009): natural and human causes and implications for water resources, ecosystems, economy, and society. *Water Resources Research*, **49**, 1040-1057.

Vinukollu, R.K., E.F. Wood, C.R. Ferguson, and J.B. Fisher, 2011: Global estimates of evapotranspiration for climate studies using multi-sensor remote sensing data: evaluation of three process-based approaches. *Remote Sensing of Environment*, **115**, 801-823.

Vörösmarty, C.J., B. Moore III, A.L. Grace, M.P. Gildea, J.M. Melillo, B.J. Peterson, E.B. Rastetter, and P.A. Steudler, 1989: Continental scale models of water balance and fluvial transport: an application to South America. *Global Biogeochem. Cycles*, **3**, 241–265, doi:10.1029/GB003i003p00241.

Vörösmarty, C.J., B.M. Fekete, M. Meybeck, and R.B. Lammers, 2000: Global system of rivers: its role in organizing continental land mass and defining land-to-ocean linkages. *Global Biogeochem. Cycles,* **14**, 599-621.

Wachtmann, R., 1975: Expansion of atmospheric temperature and moisture profiles in empirical orthogonal functions for remote sensing applications. *Digest of preprints, Topical Meeting on Remote Sensing of the Atmosphere,* Optical Society of America.

Wahr, J., M. Molenaar, and F. Bryan, 1998: Time-variability of the Earth's gravity field: hydrological and oceanic effects and their possible detection using GRACE. *J. Geophys. Res.*, **103**, 30,205-30,229.

Wahr, J., S. Swenson, V. Zlotnicki, and I. Velicogna, 2004: Time variable gravity from GRACE: first results. *Geophys. Res. Lett.*, **31**, L11501, doi:10.1029/2004GL019779.

Wang, F., L. Wang, T. Koike, H. Zhou, K. Yang, A. Wang, and W. Li, 2011: Evaluation and application of a fine-resolution global data set in a semiarid mesoscale river basin with a distributed biosphere hydrological model. *J. Geophys. Res.*, **116**, D21108, doi:10.1029/2011JD015990.

Wang, J., R. Adler, G. Huffman, and D. Bolvin, 2014: An updated TRMM composite climatology of tropical rainfall and its validation. *J. Climate*, **27**, 273-284, doi:10.1175/JCLI-D-13-00331.1.

Weedon, G.P., S. Gomes, P. Viterbo, W.J. Shuttleworth, E. Blyth, H. Österle, J.C. Adam, N. Bellouin, O. Boucher, and M. Best, 2011: Creation of the WATCH forcing data and its use to assess global and regional reference crop evaporation over land during the twentieth century. *J. Hydrometeor.*, **12,** 823-848.

Wentz, F.J., and T. Meissner, 2000: AMSR Ocean Algorithm Theoretical Basis Document. RSS Tech. Doc. 121599A-1, Remote Sensing Systems, 74 pp. [Available at http://eospso.gsfc.nasa.gov/atbd-category/38].

Willis, J.K., J.M. Lyman, G.C. Johnson, and J. Gilson, 2009: In situ data biases and recent ocean heat content variability. *J. Atmos. Ocean. Technol.*, **26**, 846-852.

Xie, X., W.T. Liu and B. Tang, 2008: Spacebased estimation of moisture transport in marine atmosphere using support vector regression. *Remote Sensing of Environment*, **112**, 1846-1855.

Yue, Q., E.J. Fetzer, B.H. Kahn, S. Wong, G. Manipon, A. Guillaume, and B. Wilson, 2013: Cloud-state-dependent sampling in AIRS observations based on CloudSat cloud classification, *J. Climate*, **26**, 8357–8377.

Zaitchik, B.F., M. Rodell, and F. Olivera, 2010: Evaluation of the Global Land Data Assimilation System using global river discharge data and a source to sink routing scheme. *Water Resour. Res.*, **46**, W06507, doi:10.1029/2009WR007811.

Zektser, I.S., L.G. Everett, and R.G. Dzhamalov, 2006: *Submarine Groundwater.* CRC Press, 466 pp.

Tables

Parameter	**Dataset Name**	**Contributing Remote Sensing Instruments**	**Key References**
Precipitation	GPCP v.2.2	SSMI, SSMIS, GOES-IR, TOVS, AIRS	Adler et al. (2003); Huffman et al. (2009)
Ocean Evaporation	SeaFlux 1.0	SSMI, AVHRR, AMSR-E, TMI, WindSat	Clayson et al. (2014)
Terrestrial Evapotranspiration	Princeton ET	AIRS, CERES, MODIS, AVHRR	Vinukollu et al. (2011)
	MERRA & MERRA-Land	MSU, HIRS, SSU, AMSU, AIRS, SSMI, ERS1/2, QuikSCAT, MODIS, GOES	Rienecker et al. (2011); Bosilovich et al. (2011); Reichle (2012)
	GLDAS	SSMI, SSMIS, GOES-IR, TOVS, AIRS, TRMM, MODIS, AVHRR	Rodell et al. (2004b)
River Runoff	University of Washington Runoff	TRMM, GOES-IR, TOVS, SSM/I, ERS, ATOVS	Clark et al. (2014)
Atmospheric Convergence	MERRA	See MERRA above	See MERRA above
	QuikSCAT Water Balance	QuikSCAT, TRMM, GRACE	Liu et al. (2006)
	PMWC v.2.0	SSMI, AMSR-E, TMI, WindSat	Hilburn (2009)
Water Storage Changes	Chambers/CSR RL05	GRACE	Chambers and Bonin (2012); Johnson and Chambers (2013); Bettadpur (2012); Tapley et al. (2004)
Precipitable Water Vapor	AIRS & AMSR-E Precipitable Water	AIRS, AMSR-E	Fetzer et al. (2006)

Table 1. Sources of data used in this study.

Continent	Coastline Length (km)	Land Area (km2)
North America	127,796	24,030,089
South America	33,956	17,737,690
Eurasia	174,833	53,234,055
Africa	41,792	29,903,956
Australia & Islands	61,387	9,045,392
Australia Mainland	20,803	7,560,766
Australasian and Indonesian Islands	40,583	1,484,627
Antarctica	41,193	12,705,364
World Land	480,957	146,656,546

Table 2. Estimated coastline length (km) and land area (km^2) for each continent and world land based on the 0.25° land mask used in this study.

Annual Mean Fluxes (mm/day)	P	P error	ET/E	ET/E error	Q	Q error	SWB Residual	Expected Closure Error	C	C error	AWB Residual	Expected Closure Error
North America	71.0	3.6	43.0	3.5	35.8	3.3	-7.8	6.1	30.4	5.8	-2.4	7.7
	73.9	**2.8**	**41.2**	**2.8**	**32.7**	**2.5**		**4.7**	**32.6**	**2.5**		**4.7**
South America	164.7	7.7	99.8	5.5	73.2	9.2	-8.2	13.2	67.0	12.9	-2.1	15.9
	166.7	**5.9**	**97.5**	**4.7**	**69.3**	**5.8**		**9.5**	**69.3**	**5.8**		**9.5**
Eurasia	72.7	4.2	41.9	6.6	34.4	4.6	-3.7	9.0	24.5	4.7	6.2	9.1
	72.3	**3.6**	**42.3**	**4.1**	**30.0**	**3.0**		**6.3**	**29.9**	**3.0**		**6.3**
Africa	70.1	3.2	55.8	4.4	12.8	1.4	1.4	5.7	12.2	2.3	2.1	6.0
	69.0	**2.6**	**56.2**	**2.7**	**12.8**	**1.2**		**4.0**	**12.8**	**1.2**		**4.0**
Australia and Islands	83.3	3.8	51.3	7.3	39.2	10.5	-7.2	13.4	47.7	9.2	-15.7	12.3
	84.5	**3.6**	**44.0**	**5.2**	**40.5**	**5.2**		**8.1**	**40.6**	**5.1**		**8.1**
Mainland Australia	50.9	2.3	39.9	5.4	14.9	4.9	-3.9	7.7	23.8	4.6	-12.7	7.5
	51.8	**2.1**	**34.0**	**3.2**	**17.8**	**2.9**		**4.9**	**17.9**	**2.9**		**4.8**
Australasian and	248.0	11.7	113.3	22.9	165.6	40.8	-30.9	48.2	177.7	34.1	-43.0	42.7
Indonesian Islands	**251.3**	**11.0**	**95.1**	**15.1**	**156.3**	**16.5**		**24.9**	**156.3**	**16.5**		**24.9**
Antarctica	18.0	4.0	1.0	0.2	17.0	4.2	0.0	5.8	19.9	3.8	-2.9	5.6
	19.1	**2.3**	**1.0**	**0.2**	**18.0**	**2.3**		**3.3**	**18.0**	**2.3**		**3.3**
World Land	78.9	4.3	48.6	4.8	33.8	4.6	-3.4	8.0	29.2	5.6	-0.2	6.7
	79.4	**3.5**	**48.2**	**3.4**	**31.3**	**3.0**		**5.7**	**31.3**	**3.0**		**5.7**
Arctic	25.8	13.0	12.7	2.1					21.8	3.3	-8.6	13.6
	34.0	**3.8**	**12.6**	**2.1**					**21.3**	**3.2**		**5.4**
North Pacific	139.2	11.3	119.7	10.5					12.8	4.2	6.7	16.0
	145.8	**6.9**	**133.1**	**6.8**					**12.8**	**3.7**		**10.4**
South Pacific	102.7	10.2	112.1	9.5					-15.3	5.4	5.9	14.9
	109.6	**6.1**	**125.1**	**6.0**					**-15.4**	**3.8**		**9.4**
North Atlantic	103.0	10.8	118.0	9.6					-18.3	6.9	3.3	16.0
	106.0	**7.7**	**124.2**	**7.4**					**-18.2**	**5.9**		**12.1**
South Atlantic	76.7	10.0	97.1	7.6					-34.3	6.3	14.0	14.0
	73.1	**6.8**	**104.9**	**6.2**					**-31.7**	**5.3**		**10.6**
Indian	105.3	10.9	120.6	11.5					-20.6	4.5	5.4	16.4
	112.6	**7.2**	**133.5**	**7.2**					**-20.9**	**3.9**		**10.9**
Carribean Sea	104.1	10.8	160.1	13.7					-49.3	7.4	-6.6	19.0
	106.9	**8.9**	**157.4**	**9.5**					**-50.5**	**6.8**		**14.7**
Mediterranean Sea	57.8	7.6	139.0	15.7					-86.9	13.0	5.6	21.8
	57.3	**7.2**	**142.5**	**10.9**					**-85.1**	**10.4**		**16.7**
Black Sea	88.2	10.2	93.7	9.5					-50.9	7.6	45.4	15.9
	69.5	**7.8**	**109.9**	**7.6**					**-40.4**	**6.7**		**12.8**
World Ocean	105.7	10.7	112.3	9.8	13.6	1.9	7.0	14.6	-12.8	5.2	6.2	15.4
	110.7	**6.1**	**123.3**	**6.1**	**12.6**	**1.2**		**8.7**	**-12.6**	**4.3**		**8.6**
World	98.0	8.9	94.2	8.4	0.0	0.0	3.9	12.2	-0.8	5.3	4.6	13.3
	101.7	**5.3**	**101.7**	**5.3**	**0.0**	**0.0**		**7.5**	**0.0**	**1.3**		**7.6**

Table 3. Observed (plain text) and optimized (bold) mean annual fluxes (mm/day) of precipitation (P), evapotranspiration (ET) or ocean evaporation (E), runoff (Q), and net atmospheric convergence (C) for the continents, major ocean basins and seas, world land, world ocean, and world. Also shown are residuals of the surface (SWB) and atmospheric (AWB) water budgets, and estimated errors on each flux and budget closure. Note that the optimization process forces the water budgets to close, hence there are no optimized residuals.

Figure Caption List

Figure 1. Mean annual fluxes (1,000 km^3/yr) of the global water cycle, and associated uncertainties, during the first decade of the millennium. White numbers are based on observational products and data integrating models. Blue numbers are estimates that have been optimized by forcing water and energy budget closure and taking into account uncertainty in the original estimates.

Figure 2. Optimized annual mean fluxes for North America (including Greenland), South America, Africa, Eurasia, the Islands of Australasia and Indonesia, mainland Australia, and Antarctica: precipitation (blue), evapotranspiration (red), runoff (green), and annual amplitude of terrestrial water storage (yellow), in 1,000 km^3/yr. The background image shows GRACE-based amplitude (maximum minus minimum) of the annual cycle of terrestrial water storage (cm).

Figure 3. Optimized mean annual cycles of precipitation (blue), evapotranspiration (red), runoff (green), atmospheric convergence (orange), and month-to-month water storage change (yellow), in mm/day, over the continents and global ocean, during roughly 2000-2010. Linear interpolation is used between monthly values. Shading indicates the uncertainty range. Note the y-axes are not uniform.

Figure 4. Optimized mean annual cycles of precipitation, evaporation, and atmospheric convergence, in mm/day, over the major ocean basins, during roughly 2000-2010. Linear interpolation is used between monthly values. Shading indicates the uncertainty range.

Figures

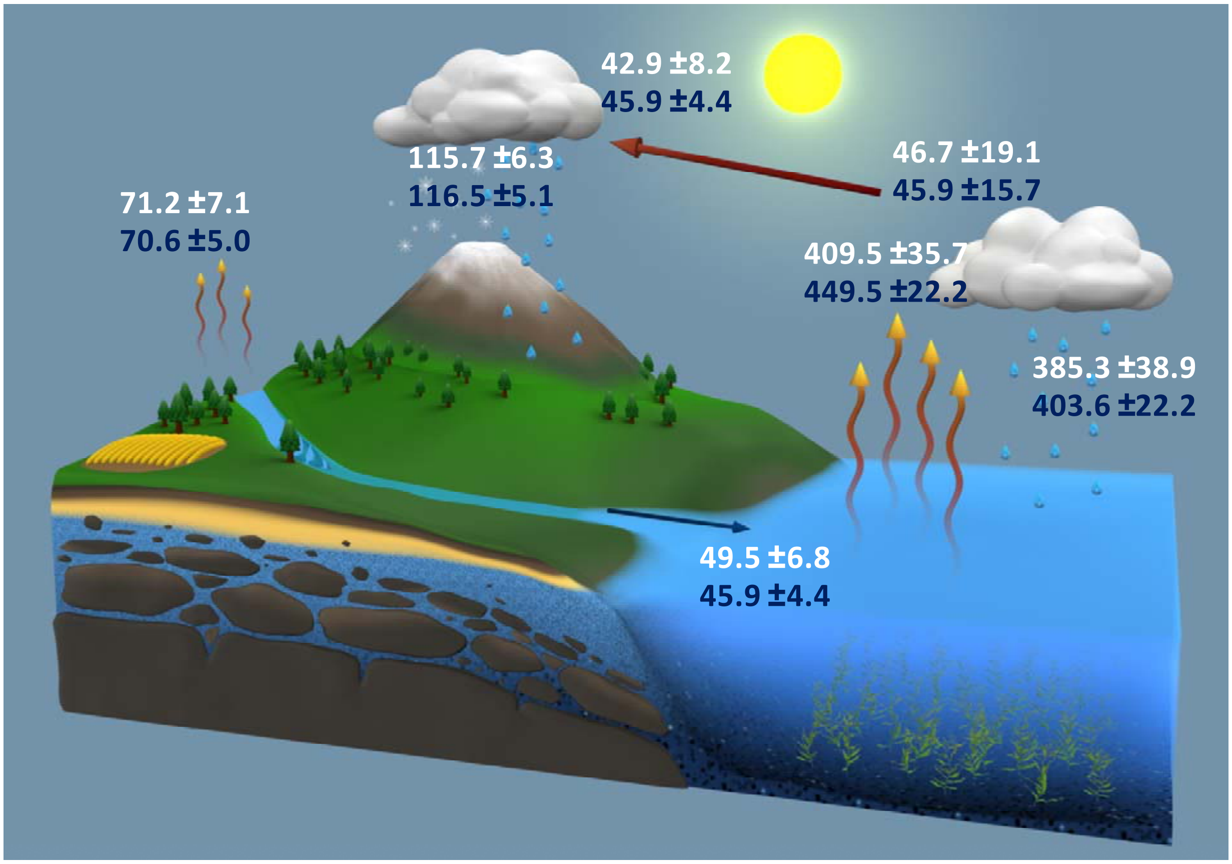

Figure 1. Mean annual fluxes (1,000 km^3/yr) of the global water cycle, and associated uncertainties, during the first decade of the millennium. White numbers are based on observational products and data integrating models. Blue numbers are estimates that have been optimized by forcing water and energy budget closure and taking into account uncertainty in the original estimates.

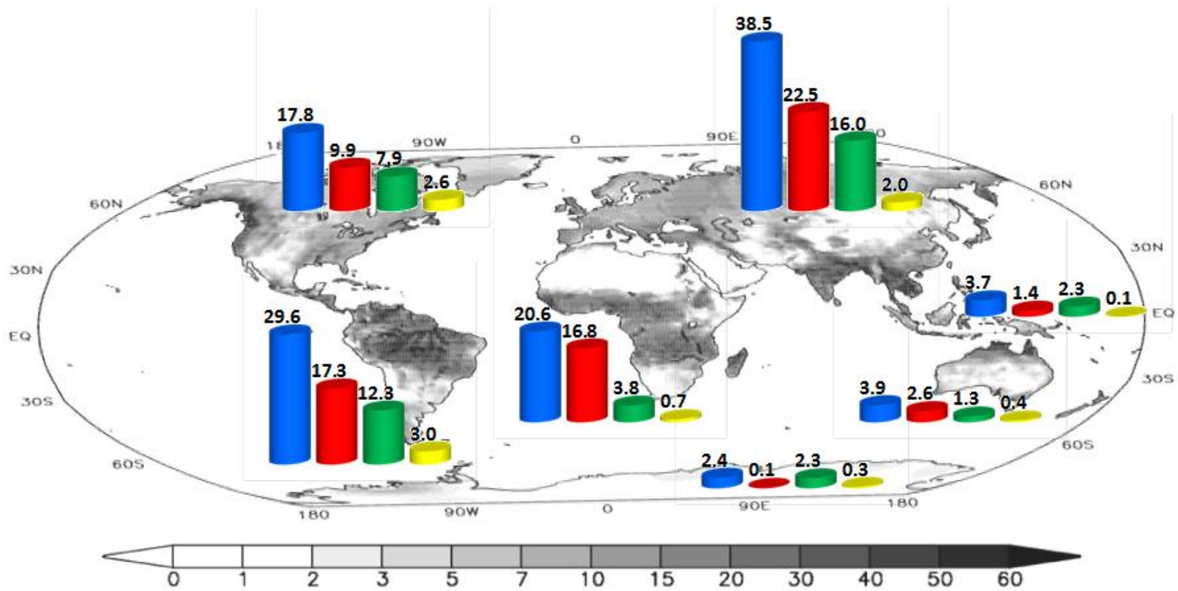

Figure 2. Optimized annual mean fluxes for North America (including Greenland), South America, Africa, Eurasia, the Islands of Australasia and Indonesia, mainland Australia, and Antarctica: precipitation (blue), evapotranspiration (red), runoff (green), and annual amplitude of terrestrial water storage (yellow), in 1,000 km^3/yr. The background image shows GRACE-based amplitude (maximum minus minimum) of the annual cycle of terrestrial water storage (cm).

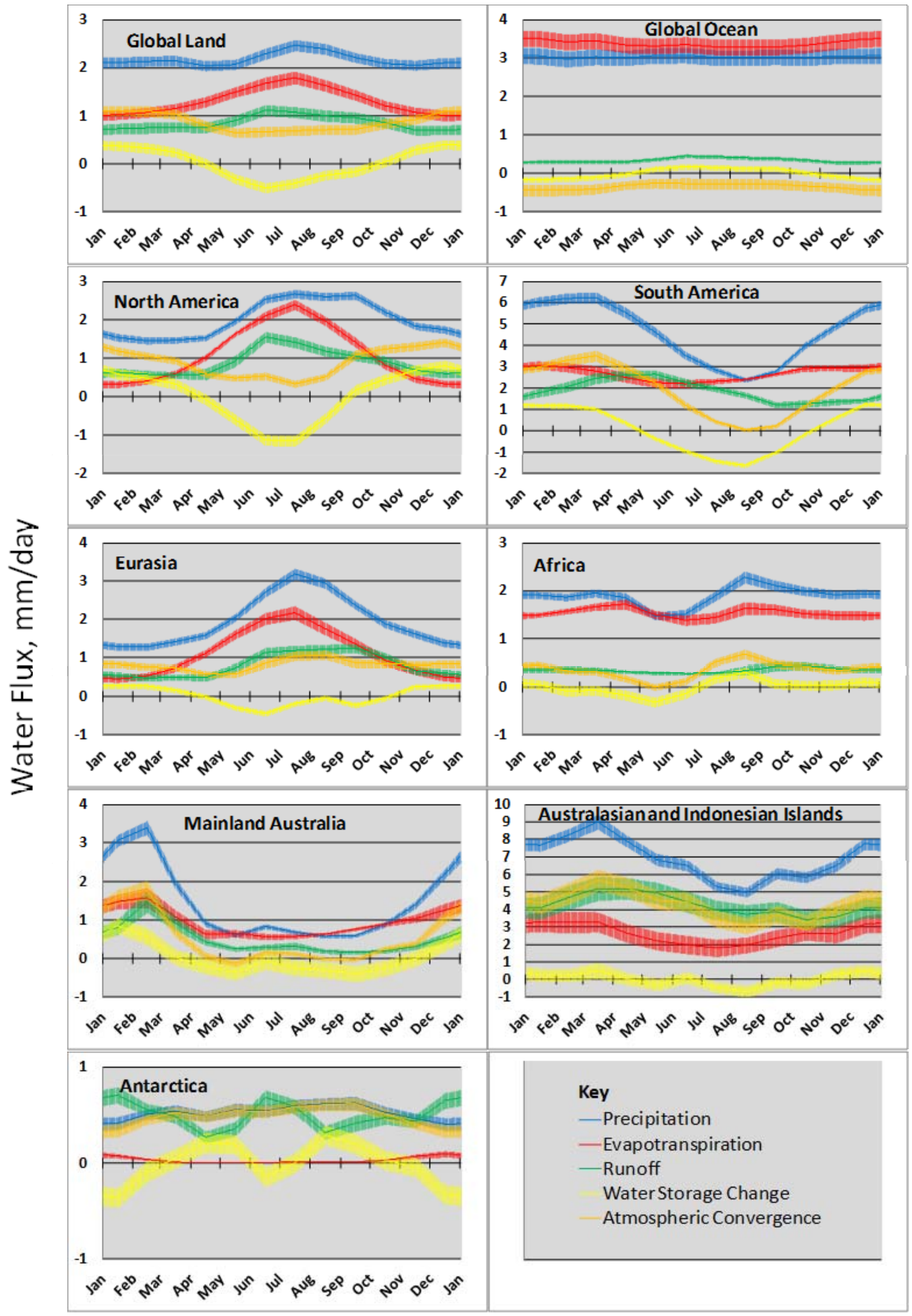

Figure 3. Optimized mean annual cycles of precipitation (blue), evapotranspiration (red), runoff (green), atmospheric convergence (orange), and month-to-month water storage change (yellow), in mm/day, over the continents and global ocean, during roughly 2000-2010. Linear

interpolation is used between monthly values. Shading indicates the uncertainty range. Note the y-axes are not uniform.

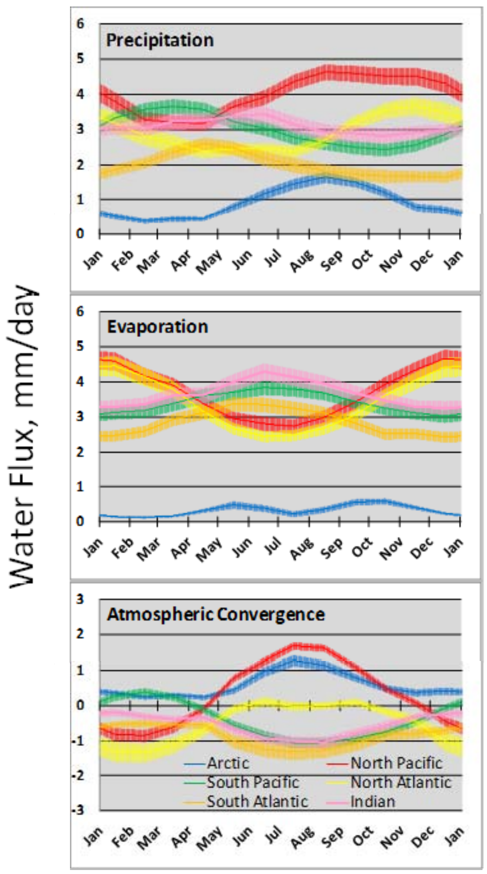

Figure 4. Optimized mean annual cycles of precipitation, evaporation, and atmospheric convergence, in mm/day, over the major ocean basins, during roughly 2000-2010. Linear interpolation is used between monthly values. Shading indicates the uncertainty range.